Research Article

High-throughput segmentation, data visualization, and analysis of sea star skeletal networks

Lara Tomholt [a,b], Daniel Baum [c], Robert J. Wood [a,d], James C. Weaver [a,d,*]

[a] *John A. Paulson School of Engineering and Applied Sciences, Harvard University, Cambridge, MA 02138, USA*
[b] *Harvard University Graduate School of Design, 48 Quincy St, Cambridge, MA 02138, USA*
[c] *Department of Visual and Data-Centric Computing, Zuse Institute Berlin, 14195 Berlin, Germany*
[d] *Wyss Institute for Biologically Inspired Engineering, Harvard University, Boston, MA 02115, USA*

A B S T R A C T

The remarkably complex skeletal systems of the sea stars (Echinodermata, Asteroidea), consisting of hundreds to thousands of individual elements (ossicles), have intrigued investigators for more than 150 years. While the general features and structural diversity of isolated asteroid ossicles have been well documented in the literature, the task of mapping the spatial organization of these constituent skeletal elements in a whole-animal context represents an incredibly laborious process, and as such, has remained largely unexplored.

To address this unmet need, particularly in the context of understanding structure–function relationships in these complex skeletal systems, we present an integrated approach that combines micro-computed tomography, automated ossicle segmentation, data visualization tools, and the production of additively manufactured tangible models to reveal biologically relevant structural data that can be rapidly analyzed in an intuitive manner.

In the present study, we demonstrate this high-throughput workflow by segmenting and analyzing entire skeletal systems of the giant knobby star, *Pisaster giganteus,* at four different stages of growth. The in-depth analysis, presented herein, provides a fundamental understanding of the three-dimensional skeletal architecture of the sea star body wall, the process of skeletal maturation during growth, and the relationship between skeletal organization and morphological characteristics of individual ossicles.

The widespread implementation of this approach for investigating other species, subspecies, and growth series has the potential to fundamentally improve our understanding of asteroid skeletal architecture and biodiversity in relation to mobility, feeding habits, and environmental specialization in this fascinating group of echinoderms.

1. Introduction

Encompassing more than 2000 extant species (Feder, 1980; Mah and Blake, 2012; Meglitsch and Schram, 1991), the sea stars (phylum Echinodermata, class Asteroidea) are perhaps one of the most quintessential marine taxa. They are globally distributed, inhabiting a great diversity of marine environments, ranging from the intertidal to the deep sea, and from polar to tropical latitudes (Feder, 1980; Mah and Blake, 2012; Meglitsch and Schram, 1991). Sea stars are usually star-shaped (the name Asteroidea originates from "asteroeidēs" meaning "star-like" in Greek), with a central disk that gradually merges into the radiating arms (or "rays"). Most sea star species have five arms, but species with more arms are equally well known, with examples including *Leptasterias aequalis* (6 arms), *Luidia maculata* (8 arms), *Pycnopodia helianthoides*

(16–24 arms), and *Labidiaster annulatus* (up to 50 arms). The asteroid body plan is typically somewhat compressed, but also shows variations, ranging from highly flattened (e.g., *Astropecten articulatus* and *Luidia clathrata*), to cushion-shaped, or nearly spherical (e.g., *Choriaster granulatus* and *Culcita* spp.) (Feder, 1980; Lawrence, 1987). Along with variations in how sharply the arms are set off from the central disk, these features have led to considerable diversity in sea star body form (Meglitsch and Schram, 1991).

The mouth of a sea star is located in the middle of the central disk, facing the substrate, thus defining the oral-aboral axis. Radiating out from the central mouth along the length of each arm is an ambulacral groove (Barnes, 1987; Feder, 1980; Meglitsch and Schram, 1991; Romanes, 1893), from which two or four rows of tube feet (or podia) protrude that are employed for locomotion, feeding, attachment to rocks

---

or prey, and - in some species - for burrowing (Barnes, 1987; Feder, 1980; Lawrence, 1987; Romanes, 1893).

The sea star body wall contains a large assembly of species-specific and morphologically distinct small calcareous skeletal elements (ossicles) held together by muscles and collagenous tissue (Blowes et al., 2017; Eylers, 1976; Lawrence, 2013; Motokawa, 1984, 2011; O'Neill, 1989). In contrast to the arms of some other echinoderms, like those of ophiuroids and crinoids, that have relatively large, serially repeating ossicle units running along the central axis of each arm (Birenheide et al., 2000; LeClair et al., 1997; Tomholt et al., 2020), asteroid arms exhibit a remarkable diversity of complex networks of ossicles enclosing an internal fluid-filled cavity, which contains the internal organs (Nichols, 1966).

The sheer complexity of these skeletal systems was eloquently described in 1898 by J. G. Wood, who stated, "*Thousands upon thousands of pure white columns are ranked in double vistas, and are overarched by an elaborate structure of the same white material on the pillars. I know nothing that can compare with this sight for delicacy and beauty. Imagine a cathedral aisle half a mile in length, which is supported by a double row of white marble columns, and whose roof is formed of the same beautiful material; then, let all the pillars be bowed towards each other in pairs, so that their capitals rest against each other, and a dim idea will be formed of the wonderful structure of the starfish*".

While these ossicles can provide a formidable protective armor (Barnes, 1987; Buchsbaum, 1947; Meglitsch and Schram, 1991), their organization also allows for arm flexibility to perform activities such as locomotion on irregular substrates, crawling into small crevices, feeding, righting, and the adoption of spawning postures (Nichols, 1966; Mah and Blake, 2012; Blowes et al., 2017; O'Neill, 1989, 1990). Arm bending and twisting is facilitated by the highly modular, and thus flexible organization of the ossicles, and via the action of circular and longitudinal muscles in the body wall (Barnes, 1987; Buchsbaum, 1947; Feder, 1980; Nichols, 1966). The asteroid body wall can also become quite rigid (Motokawa, 2011) to provide protection from the impact of waves, rocks, or the jaws and claws of predators (O'Neill, 1989), or to exert forces on their prey when feeding (Eylers, 1976; Lawrence, 1987; Meglitsch and Schram, 1991). By contracting muscles in the body wall, the ossicles are held in compression, making the framework more rigid (Motokawa, 2011; O'Neill, 1989), a mechanism which is further complemented by the presence of mutable collagenous tissues that undergo reversible stiffness changes (Eylers, 1976; Motokawa, 1984, 1985, 1988, 2011; Motokawa and Wainwright, 1991; Wilkie, 2005; Lawrence, 2013). When these connective tissues are soft, the ossicles can slide relative to one another and allow for arm movement, while, in contrast, when the connective tissues are stiffened, the ossicles are fixed in place and create a rigid body posture (Motokawa, 1985). In addition to providing arm flexibility and the capacity to modulate body wall stiffness, the intrinsic macro-scale porosity of the skeletal system also allows for gas exchange across the body wall via clusters of papulae passing through the voids between the ossicles and spines (Blowes et al., 2017; Feder, 1980; Lawrence, 1987; Nichols, 1966).

There is a high degree of skeletal variation between asteroid species, ranging from skeletal systems with closely packed ossicles that form a nearly continuous armored sheet (e.g., *Ctenodiscus australis*) to those with fewer ossicles in the aboral body wall that are arranged in a mesh-like network (e.g., *Pisaster giganteus* and *Acanthaster planci*), or those nearly devoid of ossicles on the aboral surface (e.g., *Pycnopodia helianthoides*) (Nichols, 1966; LT and JCW, personal observations). Despite this variability in asteroid internal skeletal architecture, these patterns are largely unidentifiable in living specimens, and as such, most of the species-specific ossicle features that are used for species identification purposes, relate specifically to the externally projected conspicuous surface ornamentations, such as spines, tubercles, or ridges, that adorn their aboral surfaces (Hyman, 1955).

Sea stars exhibit a great range in body size, from the tiny *Parvulastra parvivipara*, of which adults measure a mere 1 cm in diameter (Roediger

et al., 2008), to massive species like the sunflower star, *Pycnopodia helianthoides*, which can measure over a meter across (Feder, 1980). In the presence of an abundance of food, sea stars grow to large sizes relatively quickly (Sanford, 2002), which Emson (1985) hypothesized, provides a survival advantage. Conversely, sea stars can cease their growth or even decrease their body size through the resorption of their body wall when food is scarce (Lawrence, 1987; Feder, 1980; Robles, 2013). During growth, the ossicle network of sea stars grows with the animal by both enlarging existing ossicles and adding new ossicles (Eylers, 1976), the latter of which is most obvious when a sea star needs to regenerate an arm, for example after autotomy or a traumatic amputation by a predator. Each ossicle in an asteroid or other echinoderm is a single crystal of magnesium calcite (Barnes, 1987; Gayathri et al., 2007; Nichols, 1966), and is produced by skeleton-forming cells (sclerocytes) in the dermis, using ions extracted from the surrounding seawater (Barnes, 1987; Hyman, 1955; Nichols, 1966). This process results in a three-dimensional porous ultrastructure, called the stereom (Dubois et al., 1985; Smith, 1990), the periodicity of which can be extremely variable, ranging from completely disordered to highly periodic (Tomholt et al., 2020; Yang et al., 2022).

Hyman (1955) recognized the echinoderms as "a noble group, especially designed to puzzle the zoologist", and this mystification certainly applies to their skeletal anatomy: each sea star – even small individuals – can contain thousands of discrete ossicles that are arranged into elaborate network-like structures (Blowes et al., 2017; Schwertmann et al., 2019). The sheer complexity of the asteroid skeletal system is likely why its large-scale organization and biomechanical properties are still poorly understood, despite the extensive asteroid fossil record, their high biodiversity, and profound ecological importance. Moreover, the morphological details of sea star skeletal systems represent important traits for taxonomic purposes (Sladen, 1886; Fisher, 1930; Mah and Blake, 2012), so a more detailed understanding of their multi-scale organization could provide key insights into the evolutionary relationships between major asteroid taxa. In early investigations of echinoderm skeletal organization, the techniques used were limited to physically dissecting the specimen and presenting the anatomical features with hand-drawn line drawings (Eylers, 1976; O'Neill, 1989; Sladen, 1886), but these qualitative descriptions and two-dimensional representations of disarticulated skeletal systems made it virtually impossible to infer any useful information about large-scale organizational patterns. More recently, researchers have used micro-computed tomography (micro-CT) to analyze the three-dimensional organization of intact sea star skeletons (Blowes et al., 2017; Schwertmann et al., 2019), but as clearly shown in Fig. 2A, these micro-CT data sets can be notoriously difficult to interpret. As revealed from these prior studies, accurate segmentation of the CT data is essential for understanding the organizational details of the skeletal network and for elucidating the individual ossicle morphologies (Schwertmann et al., 2019). Due to the presence of thousands of individual ossicles in a single sea star, however, the *manual* segmentation of complete sea star endoskeletons (and the identification of every individual ossicle) is extraordinarily time consuming, and for all practical purposes is impossible to successfully perform within any reasonable time frame. In fact, early exploratory studies by the authors (LT, DB, and JCW) revealed that with even the most streamlined conventional workflows, this process could take years to complete, even for a moderately sized (*P. giganteus*) specimen.

Our recent development of a new, *automated* segmentation algorithm, specifically designed for investigating tesselated or highly discretized CT data sets, has addressed this limitation by making the segmentation process much more efficient (Baum et al., 2019). Using this approach, here we present the first detailed multi-scale analysis of an asteroid skeletal growth series, made possible by a new high-throughput workflow that uses micro-computed tomography, automated segmentation, data analysis and visualization tools, and additive manufacturing. This methodology, presented herein, allows for the comprehensive high-throughput analysis of sea star skeletons, providing
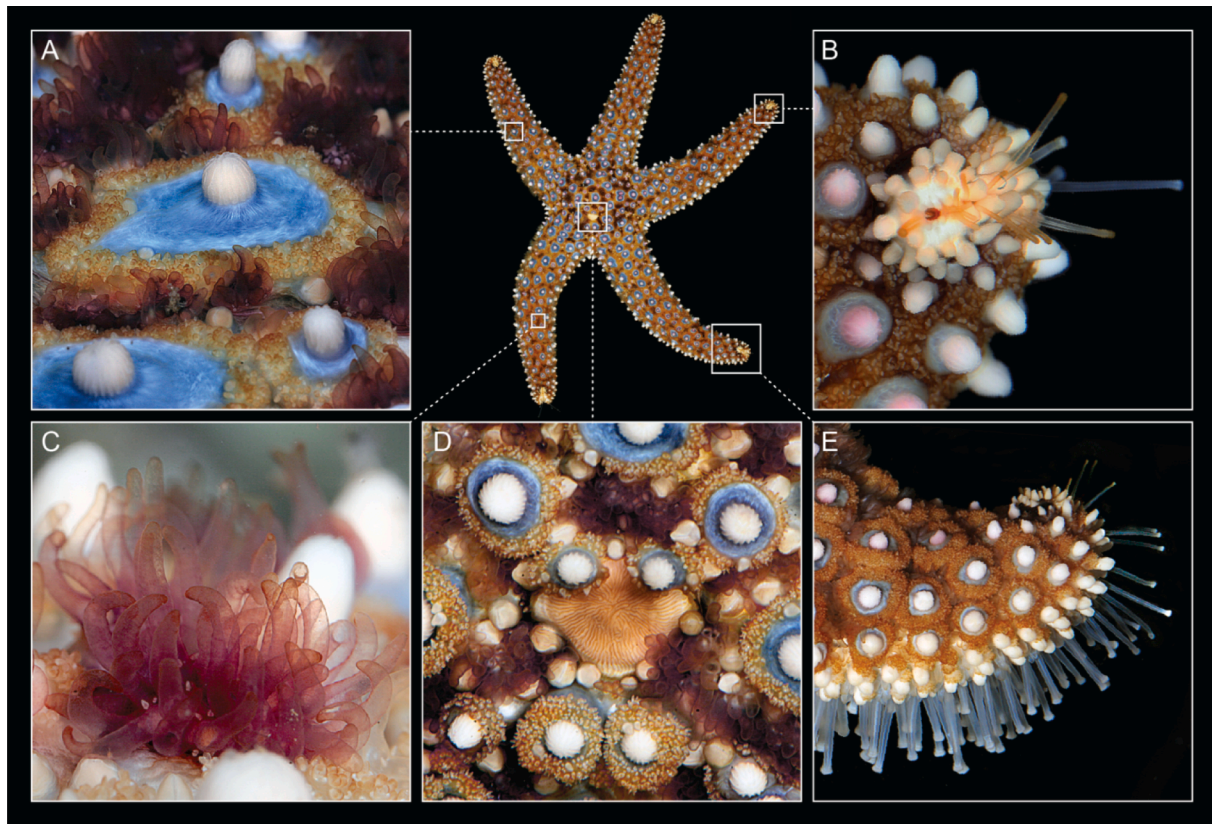
Fig. 1. Anatomical features of *P. giganteus*. A live specimen of *P. giganteus* viewed from its aboral side, clearly showing its white low-aspect-ratio blue-rimmed knob-like spines (A), the cluster of sensory elements at the tip of each arm (B), the dermal papulae (C), the madreporite (D), and the tube feet extending from the oral surface of a bent arm (E). (For interpretation of the references to color in this figure legend, the reader is referred to the web version of this article.)

a fundamental understanding of the relationship between sea star size and ossicle size, shape, count, and organization.

2. Materials and methods

2.1. Research species and specimen acquisition

The species selected for this study was the giant knobby star, *Pisaster giganteus* (Order Forcipulata) (Fig. 1). Known for its distinctive blue-rimmed, low aspect ratio spines (or "knobs"), this species inhabits the low intertidal zone and subtidal waters in coastal areas between Vancouver Island (British Columbia) and Baja California (Feder, 1980). Its large size (approaching 1 m in diameter) and its relatively high ossicle content compared to sea star species from other orders (Fisher, 1930; Gayathri et al., 2007), makes *P. giganteus* an ideal research species to demonstrate the new methodologies described in the present study.

The investigated specimens were collected from Monterey, California at 5–10 m depth. While the sampling of specimens from one specific geographical area has the potential to limit the specific size classes available for investigating growth-related changes in skeletal architecture (as was the case for the present study), it does have the benefit of largely eliminating the potential of including different subspecies that are known to exhibit differences in skeletal architecture in the comparative sample set (Hayne, 2013; Jones, 2019; Robles, 2013). Our growth series included specimens with an approximate arm tip to arm tip diameter of 36 mm (Size 1), 57 mm (Size 2), 70 mm (Size 3), and 266 mm (Size 4) (Fig. 3A), and the selected specimens did not exhibit signs of recent arm regeneration or significant structural damage.

2.2. Micro-computed tomography

Each ethanol-preserved sea star was placed in a sealed plastic bag and stabilized between two x-ray transparent foam plates to prevent specimen shift during transmission image acquisition. The specimens were scanned with an XRA-002 X-Tek HMXST225 (X-Tek, Amherst, NH, USA) micro-CT x-ray imaging system at 70 kV and 180 µA (Size 1), 75 kV and 155 µA (Size 2), 75 kV and 175 µA (Size 3), 70 kV and 180 µA (Size 4, whole animal), and 70 kV and 175 µA (Size 4, for a higher magnified view of a single arm). The generated transmission image sets were reconstructed using CT Pro software (Nikon Metrology, Brighton, MI, USA) and the corresponding image data stacks, with a voxel size of 23 µm (Size 1), 33 µm (Size 2), 39 µm (Size 3), 127 µm (Size 4, whole animal), and 70 µm (Size 4, single straight arm), were exported using VGStudio Max 3.0 (Volume Graphics, Heidelberg, Germany).

2.3. Data segmentation

The image data stacks were next imported into the AmiraZIBEdition software package version 2022.10 (ThermoFisher Scientific, Waltham, MA, USA; Zuse Institute Berlin (ZIB), Germany) and processed following the general workflow described by Baum et al. (2019), and expanded here to include additional data processing steps. No pre-processing was performed on the five data sets (i.e., four whole body scans and one high-resolution single-arm scan) prior to importation into the Amira programming environment. The first step of our data processing pipeline was binary segmentation, which uses a voxel intensity threshold to separate the structures of interest (i.e., the ossicles) from the rest of the data set, into foreground and background voxels, respectively.

The next step in the segmentation workflow was the application of a random walk distance transform on the aforementioned binary image
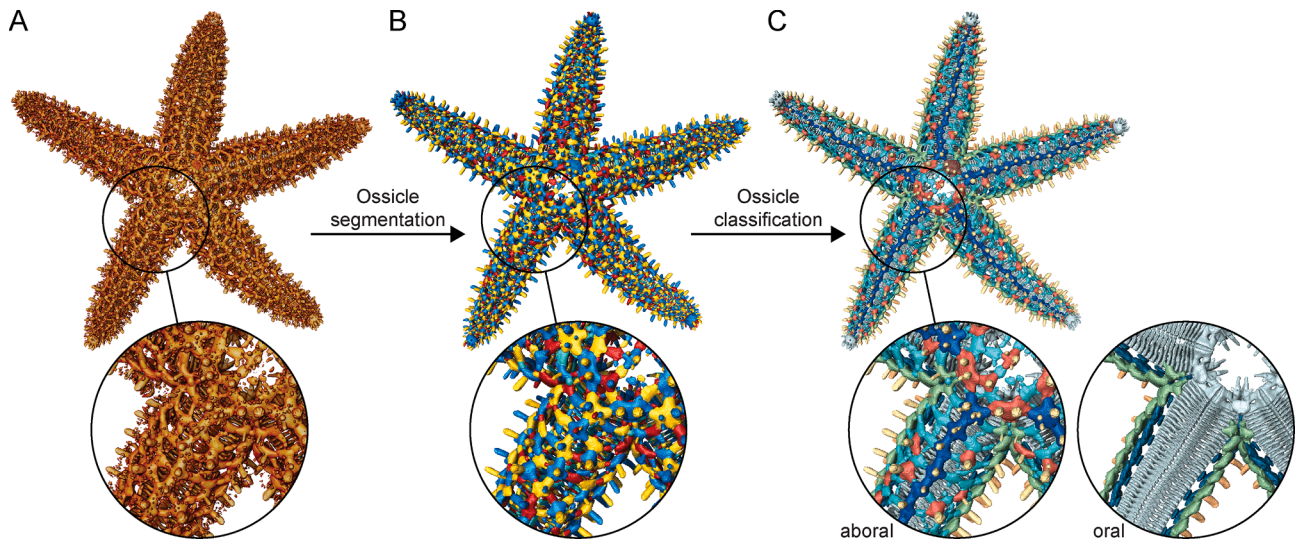
Fig. 2. Automated segmentation and ossicle-type classification workflow of a sea star's skeletal system, illustrated with the smallest *P. giganteus* specimen (Size 1) (see Fig. 3). **(A)** Surface volume rendering of the sea star endoskeleton in which the individual ossicles are barely discernible. **(B)** Using a random-walk distance-based segmentation method, the individual ossicles can be segmented, and **(C)** color-coded (cf. Fig. 5A) based on ossicle type.
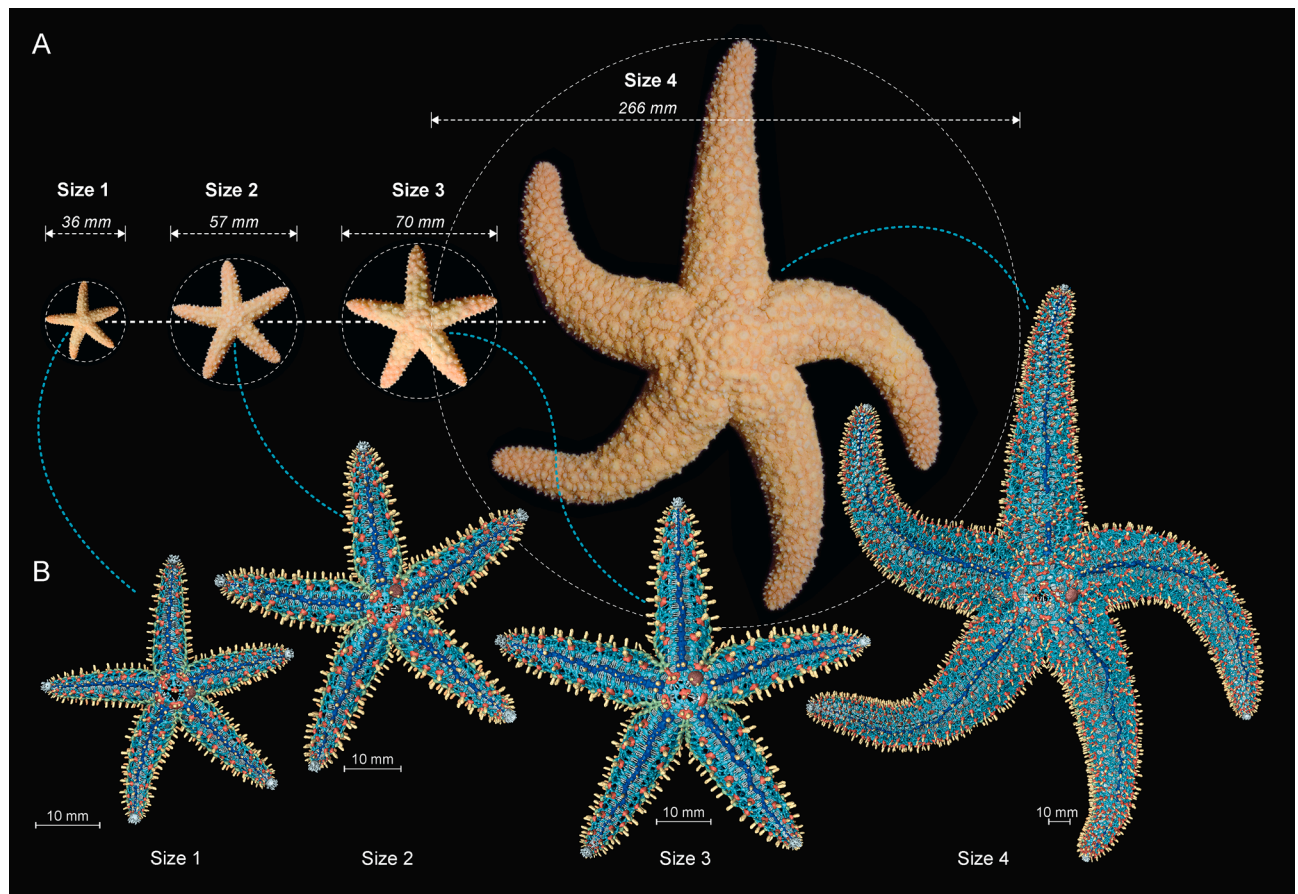

Fig. 3. Overview of the different size classes of *P. giganteus* investigated. **A.** Photographs of the four *P. giganteus* specimens, viewed from their aboral side, to scale. **B.** Aboral view of the segmented and classified endoskeletal data sets, not to scale. The aboral side of the skeleton is comprised of a network of oral marginal ossicles (OMO, blue-green), lateral marginal ossicles (LMO, green), aboral marginal ossicles (AMO, red), reticular ossicles (RO, cyan), and carinal ossicles (CO, dark blue), covered with big oral spines (OSB, light orange) and aboral lateral spines (ALS, yellow) (cf. Fig. 5A) and the madreporite on the central disk (brown). The oral skeleton contains inter alia, ambulacral ossicles, adambulacral ossicles, and small oral spines (light blue) (cf. Fig. 5A), which in these images can be seen through the gaps formed by rings of reticular and aboral marginal ossicles. (For interpretation of the references to color in this figure legend, the reader is referred to the web version of this article.)
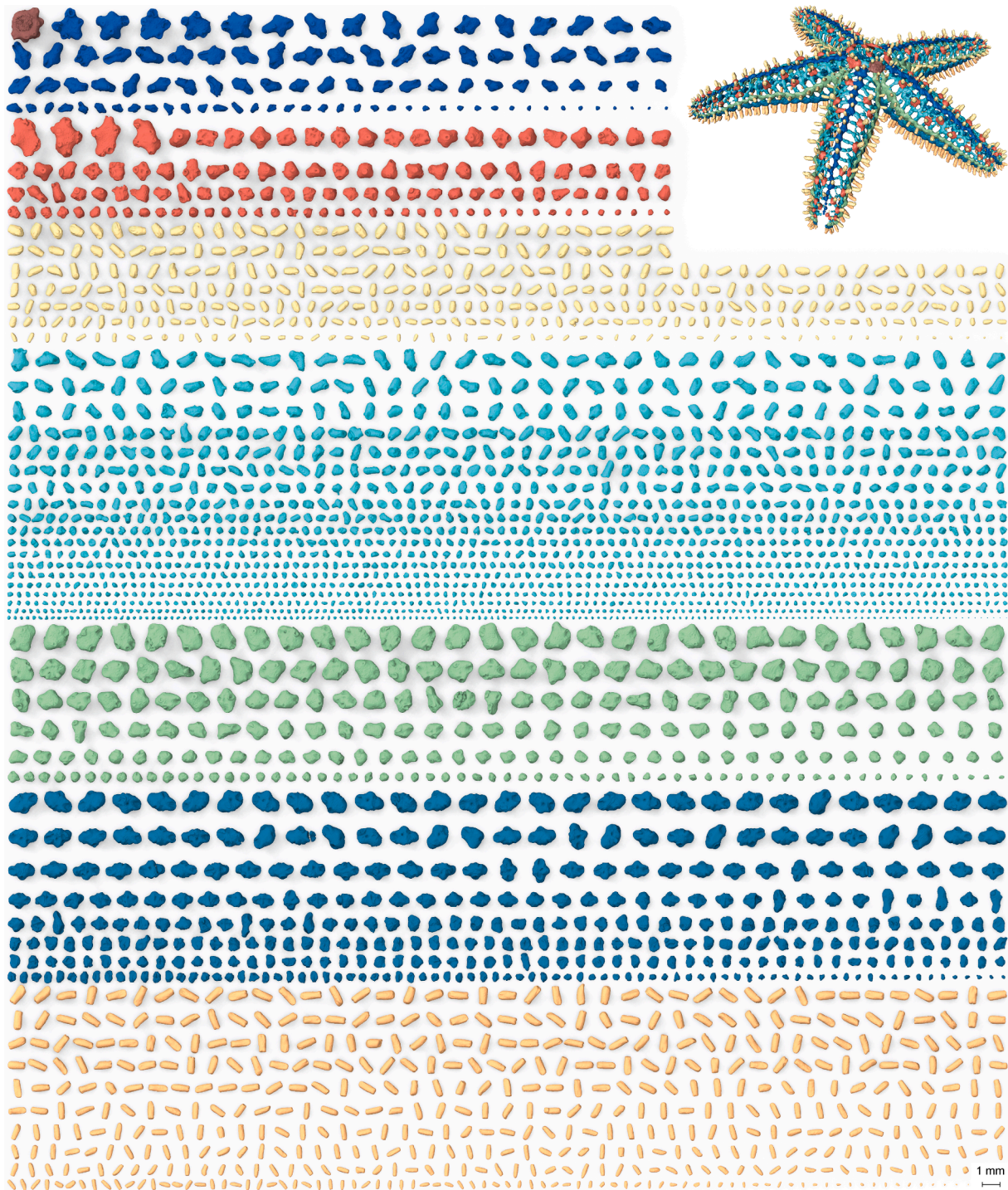
Fig. 4. Array of the 3,264 aboral ossicles present in the smallest *P. giganteus* specimen (Size 1), sorted first by ossicle type and, secondly, by ossicle volume. From top to bottom: the madreporite (brown), carinal ossicles (CO, dark blue), aboral marginal ossicles (AMO, red), aboral lateral spines (ALS, yellow), reticular ossicles (RO, cyan), lateral marginal ossicles (LMO, green), oral marginal ossicles (OMO, blue-green), and big oral spines (OSB, light orange), cf. Fig. 5AB. Each ossicle is shown from its most characteristic orientation. (For interpretation of the references to color in this figure legend, the reader is referred to the web version of this article.)

stack, which computes the average length over all random walks from each foreground voxel to the background (Baum et al., 2019). To hone in on an effective segmentation, the computation of the binary segmentation and the random-walk distance transform were repeated for multiple intensity-value thresholds, ranging from 22,000 to 30,000 (Size 1), 7,500 to 9,500 (Size 2), 10,000 to 14,000 (Size 3), and 21,000 to 26,000 (Size 4, whole animal) in steps of 10, and a single threshold of 20,400 (Size 4, single arm). For each threshold range, the random-walk distance

map was computed and normalized to the range from 0.0 to 1.0, and all resulting normalized distance maps were averaged. In contrast to using a single voxel intensity threshold, this computation of a large number of binary segmentations and their respective random-walk distance maps helped identify constrictions (narrow connections) between adjacent ossicles that were only visible for certain intensity-value thresholds. Next, the intensity values of the distance transform were used as inputs to the contour-tree segmentation algorithm, which separates the
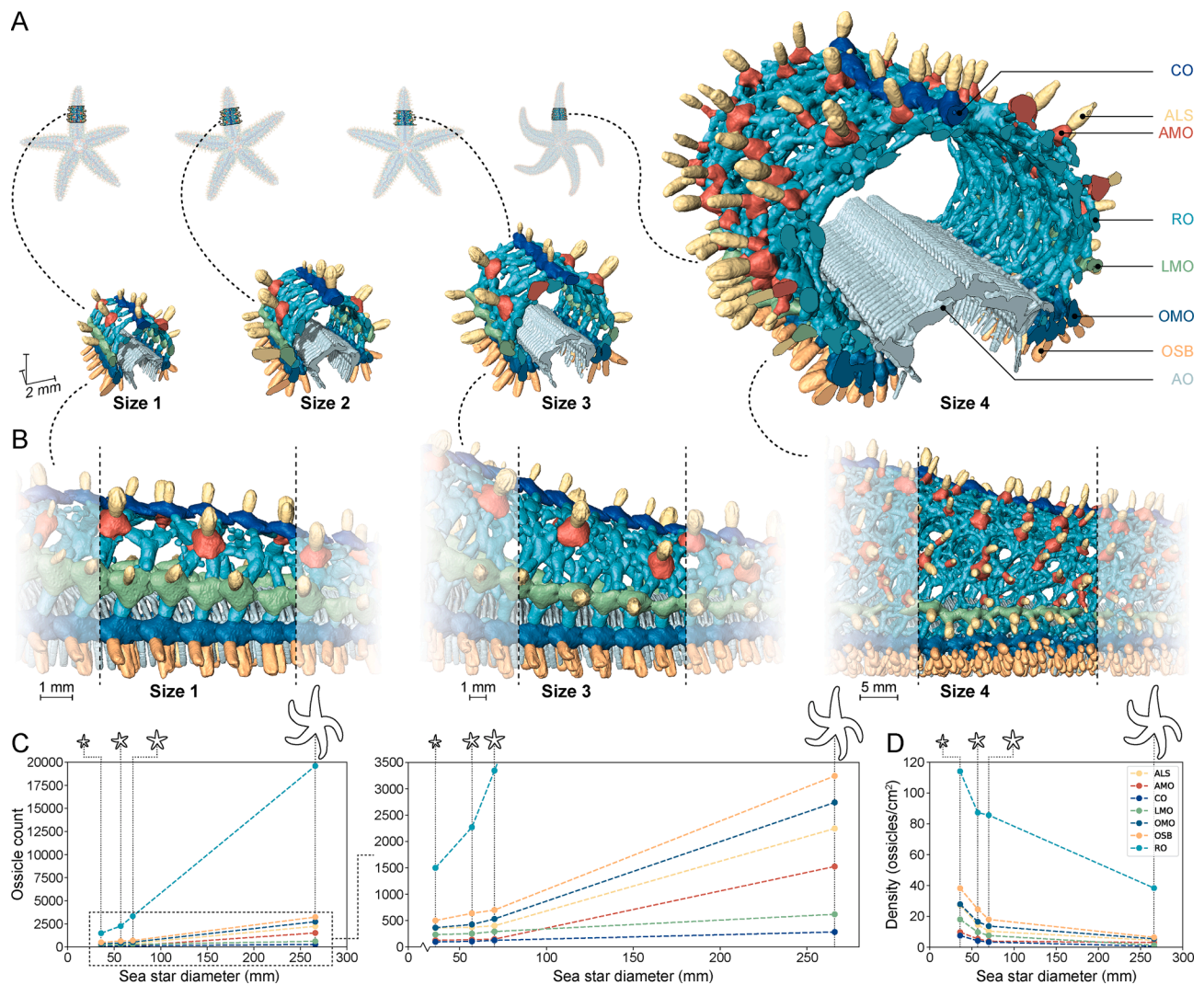
Fig. 5. Changes in ossicle quantity during sea star growth. Transversely **(A)** and laterally **(B)** viewed arm sections of each specimen clearly convey the increase in ossicle number as a sea star grows. In (A), the distal sectioned arm plane is oriented closest to the viewer (as if the camera was positioned near the arm tip). The different ossicle types distinguished in this study are the carinal ossicles (CO, dark blue), aboral marginal ossicles (AMO, red), aboral lateral spines (ALS, yellow), reticular ossicles (RO, cyan), lateral marginal ossicles (LMO, green), oral marginal ossicles (OMO, blue-green), big oral spines (OSB, light orange), and remaining oral ossicles (light blue) that include, inter alia, ambulacral ossicles (AO), adambulacral ossicles, and small oral spines. Most notable is the increase in RO quantity, forming a double, instead of a single layer reticulum by the time the sea star reaches Size 4. **C.** Plots showing changes in the total ossicle number for each ossicle type for each sea star size (indicated on the horizontal axis with the diagrammatic sea stars, to scale). The increase in reticular ossicles (RO) quantity is most conspicuous, whereas ossicles organized in single chains along (each side of) the arm, i.e., lateral marginal ossicles (LMO) and carinal ossicles (CO), increase the least in number. **D.** Plot showing the change in ossicle density (number of ossicles as a function of total sea star surface area) for each ossicle type for each sea star size. (For interpretation of the references to color in this figure legend, the reader is referred to the web version of this article.)

individual objects of interest, similar to the example shown in Fig. 2B. The result is an "imperfect" segmentation, with some objects of interest being merged with others or split into multiple pieces. This initial segmentation process took less than one hour of manual labor (including field cropping, noise reduction, etc.) and roughly eight hours of automated computation time for each data set, where most of the computation time was spent on the repeated random-walk distance transforms.

After the automated segmentation, debris and calcareous elements that were not part of the major skeletal system were removed from the data set. The latter include the pedicellariae, small pincer-like ossicles on the surface that protect the body from the settlement of fouling organisms (Barnes, 1987; Meglitsch and Schram, 1991; Romanes, 1893; Feder, 1980), and the stone canal, a calcareous tube running from the madreporite down through the central disk to the ring canal (Buchsbaum, 1947; Hyman, 1955; Romanes, 1893). Very small bits of inorganic debris (such as sand grains and related material) were removed

with the *analysis filter* module, and larger debris or damaged/misplaced ossicles and pedicellariae were removed with the *pick and merge labels* module. To develop a more accurate segmentation from the aforementioned "imperfect" segmentation, under-segmented ossicles were manually split with the segmentation editor, and over-segmented ossicles were merged using the *pick and merge labels* module. These postprocessing steps took between roughly three and 60 h, depending on the size of the sea star, the quality of the micro-CT data, and the features of interest, with smaller sea stars and higher-quality micro-CT data sets requiring less time.

The segmented ossicles were then manually classified and colorcoded based on their morphology, position, and their adjacent ossicles (Fig. 2C), although additional coding steps using a Random Forest Classifier (Breiman, 2001) and other shape descriptor-based algorithms were also employed for automating this process. The ossicle types identified and analyzed in this study are the madreporite, aboral lateral
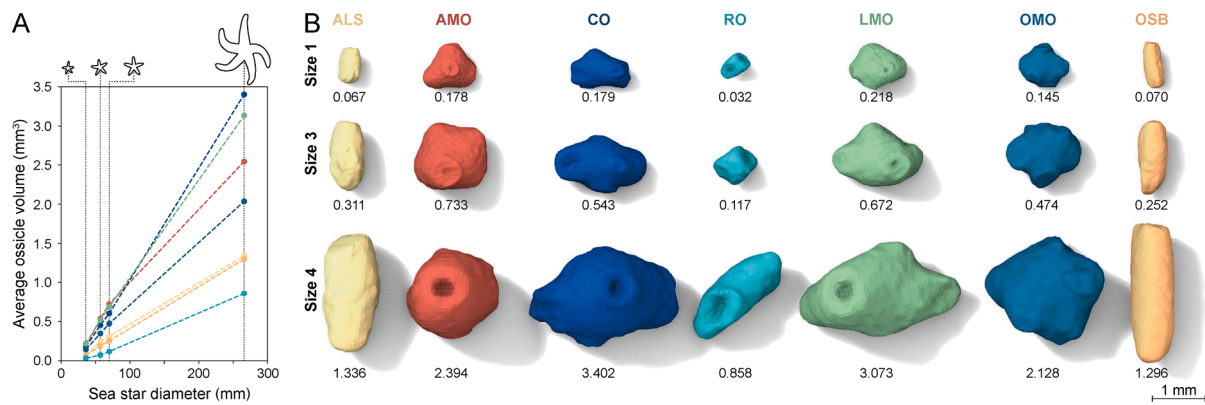
Fig. 6. Changes in average ossicle volume for each ossicle type. **A.** Plot showing average ossicle volume changes during sea star growth. **B.** Representatives of each ossicle type (cf. Fig. 5A) of average volume, selected from the data sets of Size 1, Size 3, and Size 4, are visualized to scale, with each ossicle's volume (in mm³) noted below its corresponding ossicle.

spines (ALS), aboral marginal ossicles (AMO), carinal ossicles, (CO), reticular ossicles (RO), lateral marginal ossicles (LMO), oral marginal ossicles (OMO), big oral spines (OSB), and others (including, inter alia, ambulacral ossicles, adambulacral ossicles and small oral spines). Classification of each whole sea star data set required between two and 30 h to complete, depending on the size of the imaged sample, with smaller sea stars requiring less time. Given the complexity of the skeletal systems, some of the data cleaning steps (as described in the previous paragraph) were also performed subsequent to ossicle classification.

From these segmentation and classification workflows, several key lessons were learned that would significantly accelerate these approaches in future iterations. The first topic relates to the quality of the CT-scanned specimens. Before CT data collection, care should be taken to ensure that the scanned specimen lacks significant physical damage such as crushed or otherwise fragmented ossicles, and is as free as possible from electron-dense foreign debris. These criteria can generally be evaluated either through an initial visual inspection of the specimen, or from the preliminary acquisition of various single x-ray transmission images. Furthermore, the choice of specimens should exclude those that exhibit significant arm twisting or bending as these can impact local x-ray transparency by over- or under-exposing sections of the skeletal system, complicating the implementation of specific thresholding operations during the segmentation process.

The second topic relates to the quality of the acquired CT data set in order to produce satisfactory automated segmentation results. Several factors need to be taken into consideration during CT data acquisition to obtain high quality scans, of which the two main criteria are discussed here. The first relates to the stability of the specimen during data acquisition. To address these concerns, particular care was taken when mounting the specimens, which included maintaining them in a hydrated state, and the manufacturing of custom foam blocks in which sea star-shaped cavities were excavated in order to completely immobilize each specimen during the scanning process. The second relates to the ratio of the minimum feature size of interest (in this case a single ossicle) to the maximum scanned field of view (in the examples presented here, either the entire sea star, or an individual arm, since the resolution of the micro-CT data affects the segmentation quality. In lower resolution data, for example, constrictions with soft tissue (characterized by lower electron density) between adjacent ossicles may no longer be visible, and thus boundaries between adjacent ossicles might not be identified by the random-walk distance transform algorithm. Thus, the algorithm may produce more under- or over-segmented ossicles depending on the intensity value threshold(s), and more manual proofreading and corrections may be required, such as was the case in this study with the data set acquired from the largest sea star (Size 4). In contrast, high-resolution micro-CT data may reveal the ossicles' stereom structure, which, due to its porous nature, has shown to mislead the segmentation

of ossicles in other echinoderm data sets (LT, DB, and JCW, personal observations). In summary, three parameters should thus be taken into consideration in order to obtain an appropriate resolution of micro-CT data for automated segmentation: the size of the specimen to be scanned, the detector resolution, and the minimum feature size to be distinguished.

The third topic relates to data processing. As previously pointed out by Blowes et al. (2017), the overall level of X-ray absorption in the ambulacrum is much higher than in the aboral body wall, consistent with the presence of the regular and densely packed rows of ambulacral ossicles (see Fig. 2C magnified oral and aboral views). The result of this disparity in average electron density is that the intensity-value threshold of the random-walk distance transform can only be optimized for either the aboral, lateral, and oral ossicles, or the ambulacral and adambulacral ossicles, and, consequently, the computed random-walk distance map leads to under-segmentation of the first or over-segmentation of the latter. To address this limitation, the data set can be divided into distinct regions of interest, processed using varying intensity thresholds, and then recombined.

2.4. Data analysis and visualization

The segmented and classified data sets were subsequently converted into surfaces, using Amira's fast algorithm with unconstrained smoothing (with a smoothing extent of two), and the resulting images were exported for comparative analysis (Fig. 2, Fig. 3B, Fig. 5AB, Fig. 7, Fig. 8, and Fig. 9). The centerpoint of each sea star was estimated by positioning a sphere in the sea star's central disk and extracting its coordinates using Amira's *Create Sphere* module. The normals of a plane at that centerpoint and perpendicular to the axis of a single straight arm were estimated using the *Slice* module. Numeric data on each individual ossicle, including volume, elongation (the ratio of the medium and largest eigenvalue of the covariance matrix), flatness (the ratio of the smallest and medium eigenvalues of the covariance matrix), position (barycenter coordinates), and network connectivity data (node coordinates and connections), were extracted and exported as CSV files.

The CSV files were then imported into our Python scripts for further data analysis and visualization, which included the total number of ossicles per ossicle type (Fig. 5C), ossicle density (Fig. 5D), average ossicle volume per ossicle type (Fig. 6A), ossicle parameter value distribution (Fig. 8 and Fig. 9AB), ossicle connectivity between different ossicle types (Fig. 10B), the generation of scatter plots to identify potential relationships between two ossicle properties (Fig. 7, Fig. 8, Fig. 9BC, and Fig. 11A), and the calculation of the distance between each ossicle barycenter and the aforementioned plane (Fig. 7, Fig. 8, and Fig. 9BC). Subclassification of the ossicle types was performed with scikit-learn's (Pedregosa et al., 2011) support vector classification and agglomerative
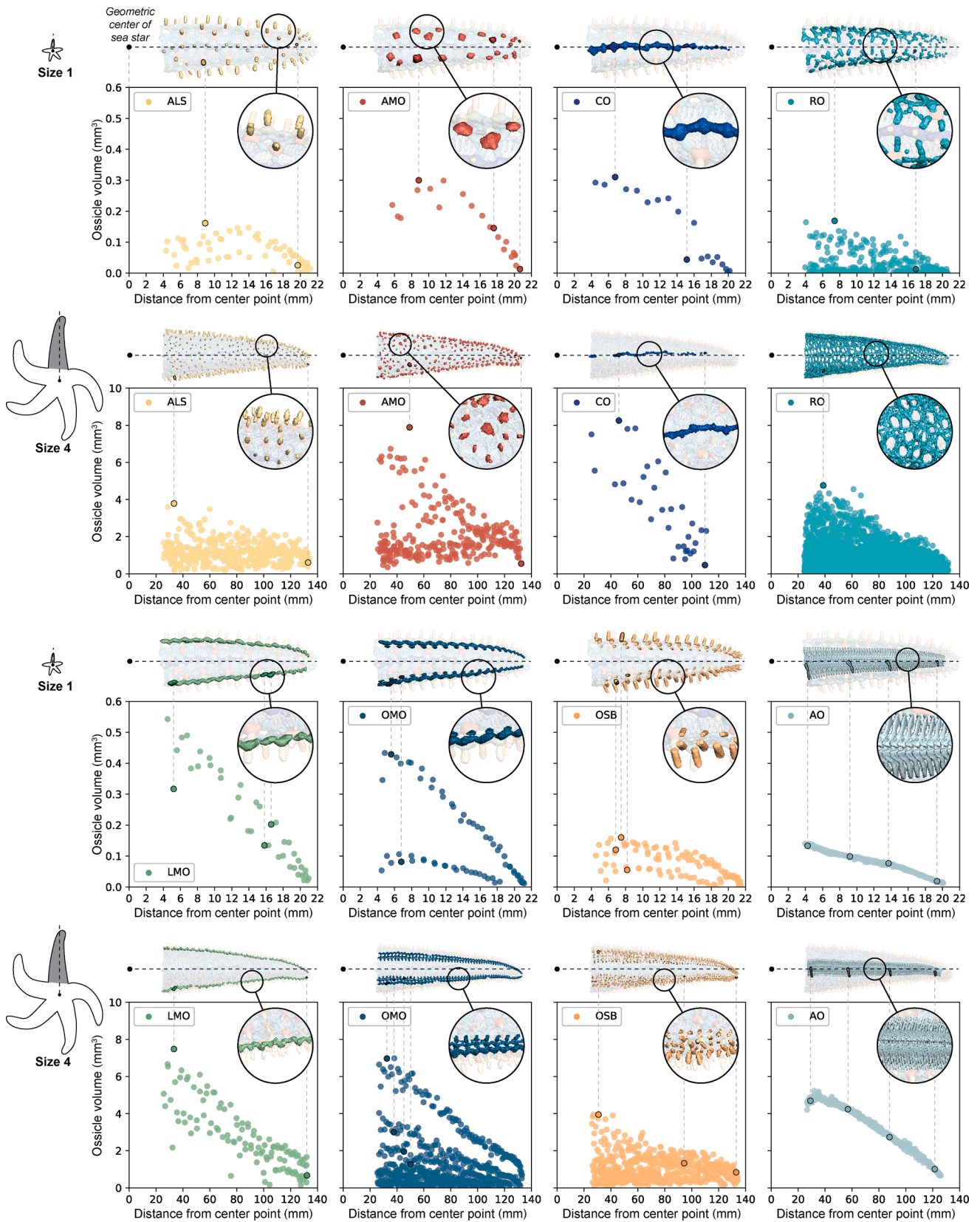
Fig. 7. Location-specific variability in individual ossicle volume. Ossicle volume as a function of the ossicle's distance along the arm axis from the sea star's geometric center for each ossicle type from Size 1 and Size 4 sea stars. The data are shown as scatter plots and include aboral views of the respective ossicles in the arm with the specified arm axis (dotted line) and the geometric center point of the sea star (black dot at the start of the dotted line). For each ossicle type and sea star size, several individual ossicles are highlighted in both the plots and arm views. These plots illustrate how some ossicle types exhibit clear relationships between ossicle location and volume (e.g., AO), whereas others only show trends in the Size 1 sea star, and the trends become less conspicuous in the Size 4 sea star (e.g., AMO), and some ossicle types only show a trend in the upper boundary (e.g., RO).
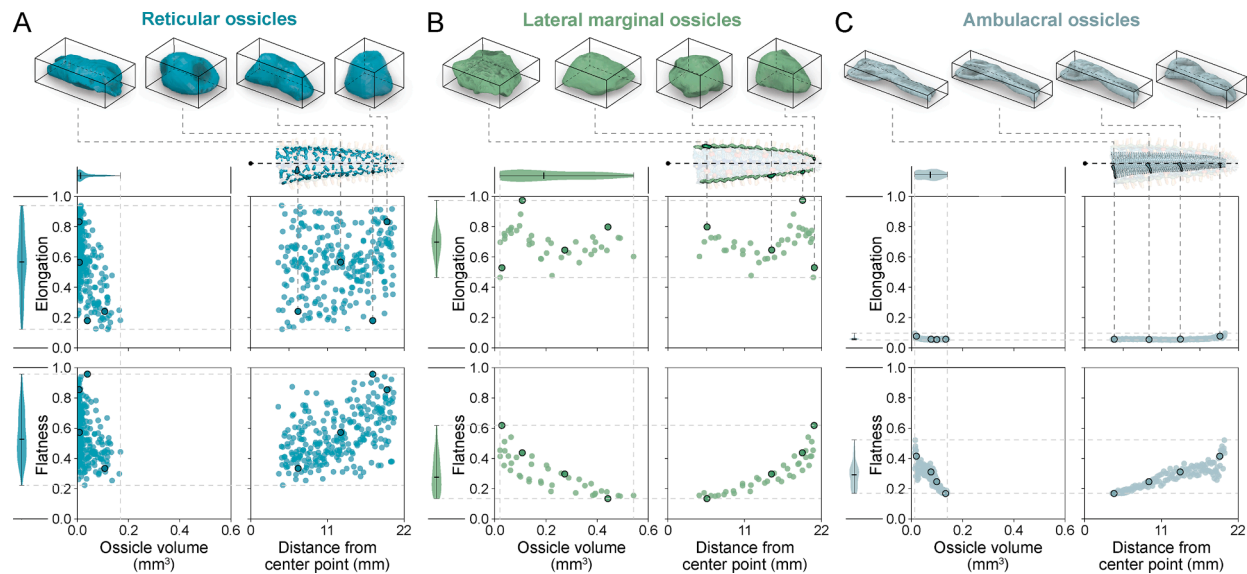
Fig. 8. Variability in shape and volume of three ossicle types in a single arm of Size 1 (cf. Fig. 7), with the medial arm axis (dotted line) and geometric center point of the sea star (black dot) denoted. The locations of each of the four ossicle examples of each ossicle type are indicated, and are displayed in their corresponding bounding boxes as isometric views (not to scale). **A.** The reticular ossicles (RO) show high variation in shape and volume, and as such, their scatter plots do not reveal any obvious trends. **B.** Lateral marginal ossicles (LMO) show less variation in shape than the reticular ossicles (cf. A), and exhibit a relatively clear relationship between ossicle flatness and volume or ossicle location. **C.** The geometry of the ambulacral ossicles (AO) remains relatively consistent along the arm.

clustering (average linkage) algorithms (Fig. 9BC). Results from these analyses were further used to identify individual ossicles of interest to illustrate the quantitative findings (Fig. 6B, Fig. 7, Fig. 8, Fig. 9B, Fig. 10B, Fig. 11).

Additional visualizations of the data sets were created using the 3D modeling software Rhinoceros 6.0 and its Grasshopper plug-in (Robert McNeel & Associates, Seattle, WA, USA). The surfaces generated in Amira were exported to DXF files, which were subsequently imported into the Rhinoceros environment as meshes. The versatility of the rendering environment of Rhinoceros allowed us to carefully balance the use of light and shadows to create images that provided critical insights into the size of individual ossicles and growth trends (Fig. 6B), and ossicle shape and smaller-scale morphological features (Fig. 8, Fig. 10B, and Fig. 11B). In addition, the imported ossicle meshes allowed for the estimation of each whole-animal's surface area for ossicle density analysis (Fig. 5D) using Grasshopper's 3D convex hull component. Using the Grasshopper plugin, we also developed a script for the rapid sorting and arrangement of all the individual ossicles present in a single sea star on a two-dimensional grid. In this multi-step process, the native 3D orientations (x, y, z, tilt, and rotation) of each ossicle in the articulated skeletal system were initially preserved. Variation in z location was collapsed to a single 0 value, positioning all of the ossicles on a single x-y plane, while preserving each ossicle's natural orientation. Subsequently, any out-of-plane ossicle tilting was removed, resulting in a planar orientation. In a final step, the ossicles were sorted by type and volume and arranged along a periodic grid structure, and displayed in plan view (Fig. 4).

To gain an understanding of the connectivity of the ossicles, a region adjacency graph was created from the segmented ossicles of the smallest sea star (Size 1) in the Amira software, selecting a neighborhood of six (i. e., two voxels of distinct ossicles sharing a face) to establish a connection between adjacent ossicles. These ossicle connection data were exported to CSV files, which, in turn, were imported into a separate Grasshopper script. The script linked the connectivity data to the ossicle meshes based on their barycenter coordinates, and visualized ossicle connectivity by color-coding the ossicles (Fig. 10A, middle image), and created a three-dimensional graph-like network with color-coded nodes of weighted size based on their connectivity (Fig. 10A, right image, Fig. 10B, and Fig. 11B).

2.5. Ossicle network flexibility

Beyond the identification, classification, and spatial mapping of specific ossicle types, we can also develop data processing workflows to gain new insights into the ossicle connectivity relationships that govern multi-directional sea star arm motion. To investigate these effects, the Grasshopper plug-in, which also allows for parametric modeling of complex 3D geometries (Frølich et al., 2017), was employed to develop a parametric script that generated a connected, yet flexible model from the individual ossicle surface volumes and ossicle connection data obtained with the Amira software. The Grasshopper script allows the user to select a region of the skeletal system, manually remove or join small adjacent ossicles (in this study, to generate a 30X scale model, generally those with an original volume smaller than ca. 0.02 mm³), and, where necessary, remove, add, or reroute ossicle connections. The ossicles were individually smoothed and scaled by a factor 0.95, to ensure sufficient space between them. For each ossicle-ossicle connection, the script identified the location at which two ossicle geometries meet, placed a ball-and-socket joint at that location, and fused the joint with the associated ossicle volumes. The balls (Fig. 12A, displayed in purple) had a diameter of 4 mm and the sockets (Fig. 12A, displayed in white) had a thickness of 1 mm, with a space of 0.5 mm between them. The resulting models were subsequently printed on a Connex500 (Stratasys, Eden Prairie, USA) inkjet-based 3D printer (Fig. 12), in order to investigate the impacts of ossicle geometry on skeletal flexibility and range of motion.

3. Results

3.1. Ossicle type classification and organization

The raw micro-CT data sets and volume renderings of the mineralized skeletal network provide little clarity regarding ossicle organization (Fig. 2A). Even after ossicle segmentation, when individual ossicles are clearly distinguishable from one another, the skeletal structure of *P. giganteus* remains seemingly disorganized (Fig. 2B). Yet, upon classification and subsequent color coding, ossicle organization patterns became apparent (Fig. 2C and Fig. 3B), and the highly regular fashion in which each ossicle type articulates was revealed. While the basic
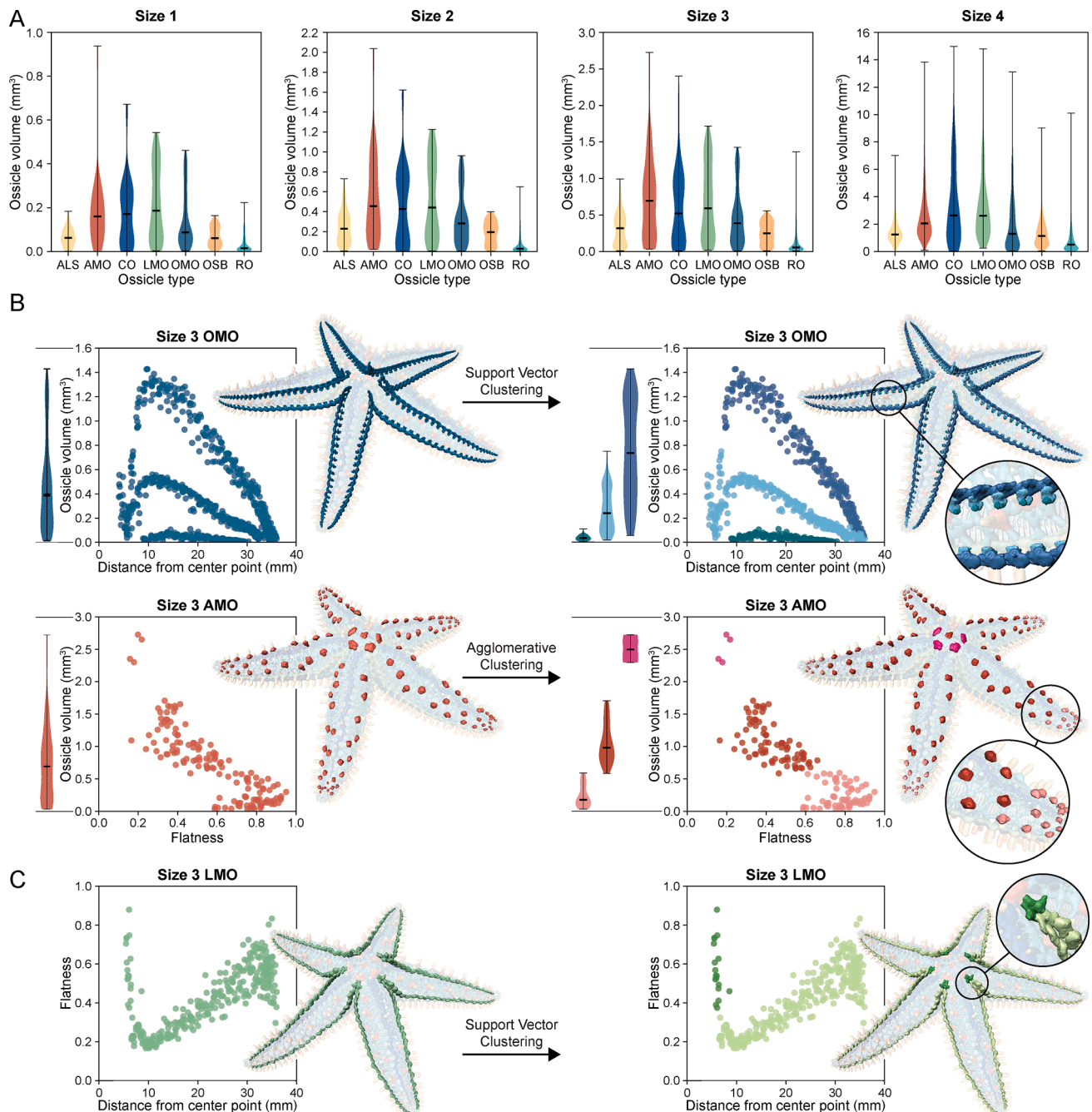
Fig. 9. Property-based ossicle subclassifications. **A.** Violin plots of ossicle volumes for each ossicle type (or class) in each sea star size often demonstrate multimodal distributions, suggesting the existence of distinct ossicle subclasses. **B.** Sub-classification with clustering algorithms, based on ossicle volume and location for the oral marginal ossicles (OMO), and on ossicle volume and shape (flatness) for the aboral marginal ossicles (AMO). Perspective views of the sea star denote the location of the ossicles in each (sub)class. Violin plots show the ossicle volume distribution for each (sub)class, and the scatter plots show the data for two different ossicle properties. OMOs are organized into three rows on each side of the arm, with each subclass occupying an individual row. The three subclasses identified in AMO are the four large ossicles at the central disk (bright pink), the larger ossicles at the central disk and the proximal regions of the arms (dark red), and the smaller ossicles at the distal regions of the arms (light pink). **C.** Sub-classification of lateral marginal ossicles (LMO) into two groupings based on ossicle shape (flatness) and location (distance from the sea star center point). The algorithm identified ossicles in the armpits (dark green) – that don't follow the same trend as the other ossicles (light green) – as a different subclass. (For interpretation of the references to color in this figure legend, the reader is referred to the web version of this article.)

asteroid skeletal structure has been described previously (Blowes et al., 2017; Eylers, 1976; Hyman, 1955; Meglitsch and Schram, 1991; Nichols, 1966; O'Neill, 1989; Romanes, 1893; Schwertmann et al., 2019; Wood, 1898), this study's classified data sets on whole sea stars allowed us to understand and describe in detail the sea star's skeletal structure and identify distinct ossicle types based on newly revealed ossicle organizational patterns.

The nomenclature of different ossicle types in this study largely follows those used by other echinoderm and asteroid researchers in the field. Moreover, given that within the order Forcipulata, sea star skeletal organization shows little variation (Eylers, 1976), descriptions of sea star skeletal structures and ossicle classifications on species within this
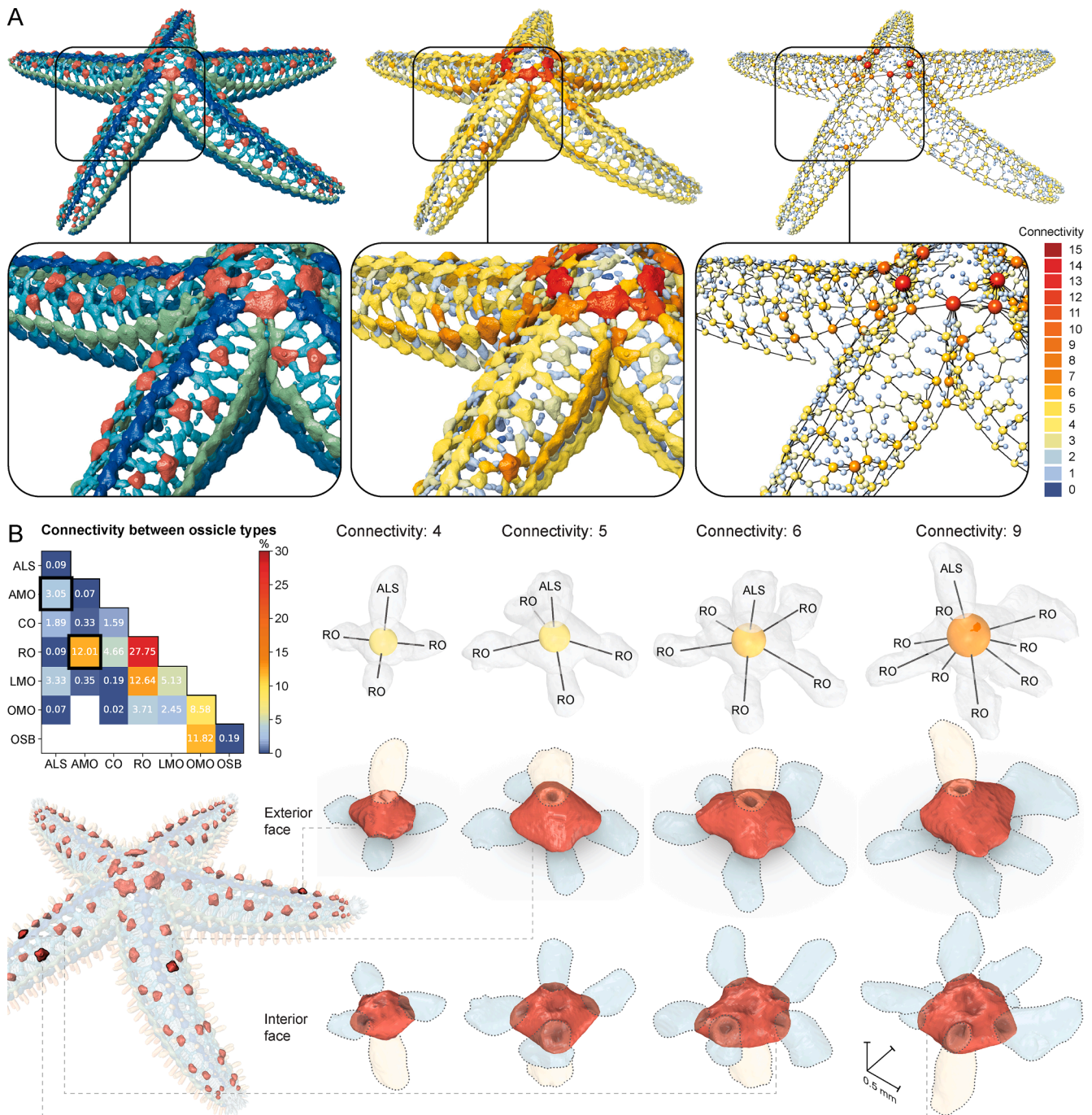
Fig. 10. Ossicle connectivity and their related sub-ossicle-scale morphological features. **A.** Perspective views of the full Size 1 aboral skeleton, excluding the aboral lateral spines (ALS), big oral spines (OSB), and the madreporite. Classified ossicles (left, for color-coding cf. Fig. 5A), ossicles color-coded by connectivity (middle), and color-coded ossicle nodal connectivity map, represented by spheres of weighted size positioned at the barycenter of each ossicle and connected to adjacent ossicles with lines (right). **B.** Heat map showing the percentage of the sea star's total number of connections between each ossicle type (top left), revealing, inter alia, the majority of ossicle connections within the sea star connect reticular ossicles with one another, with the two most common connections for aboral marginal ossicles, i.e., AMO-ALS and AMO-RO, outlined with a black border. Representative AMO ossicles of connectivity 4, 5, 6, and 9 shown to scale in axonometric views, with their connectivities represented by color-coded spheres of weighted size (cf. Fig. 10A) (top row), their exterior faces exhibiting depressions at the position of aboral lateral spines (middle row), and their interior faces exhibiting depressions at the position of reticular ossicles (bottom row).

order (Barnes, 1987; Blowes et al., 2017; Buchsbaum, 1947; Eylers, 1976; Hyman, 1955; Lawrence, 1987; Meglitsch and Schram, 1991; Nichols, 1966; Romanes, 1893; Schwertmann et al., 2019) are similar to those of *P. giganteus* presented herein. The ossicles have often been named after their position on the body (e.g., marginal ossicles), their arrangement (e.g., reticular ossicles), and/or their function (e.g., spines), and any newly introduced descriptors in this study follow the

same practice.

The asteroid skeletal structure can be divided into the oral and aboral skeleton. The oral skeleton of *P. giganteus*, much like those of other asteroid species, can be distinguished by the dense and repetitive arrangement of the ambulacral ossicles (AO) along the arms (Fig. 2C, Fig. 5A, and Fig. 7). The rows of ossicles, one on each side of the arm, are slightly tilted in the direction of the central disk (Schwertmann et al.,
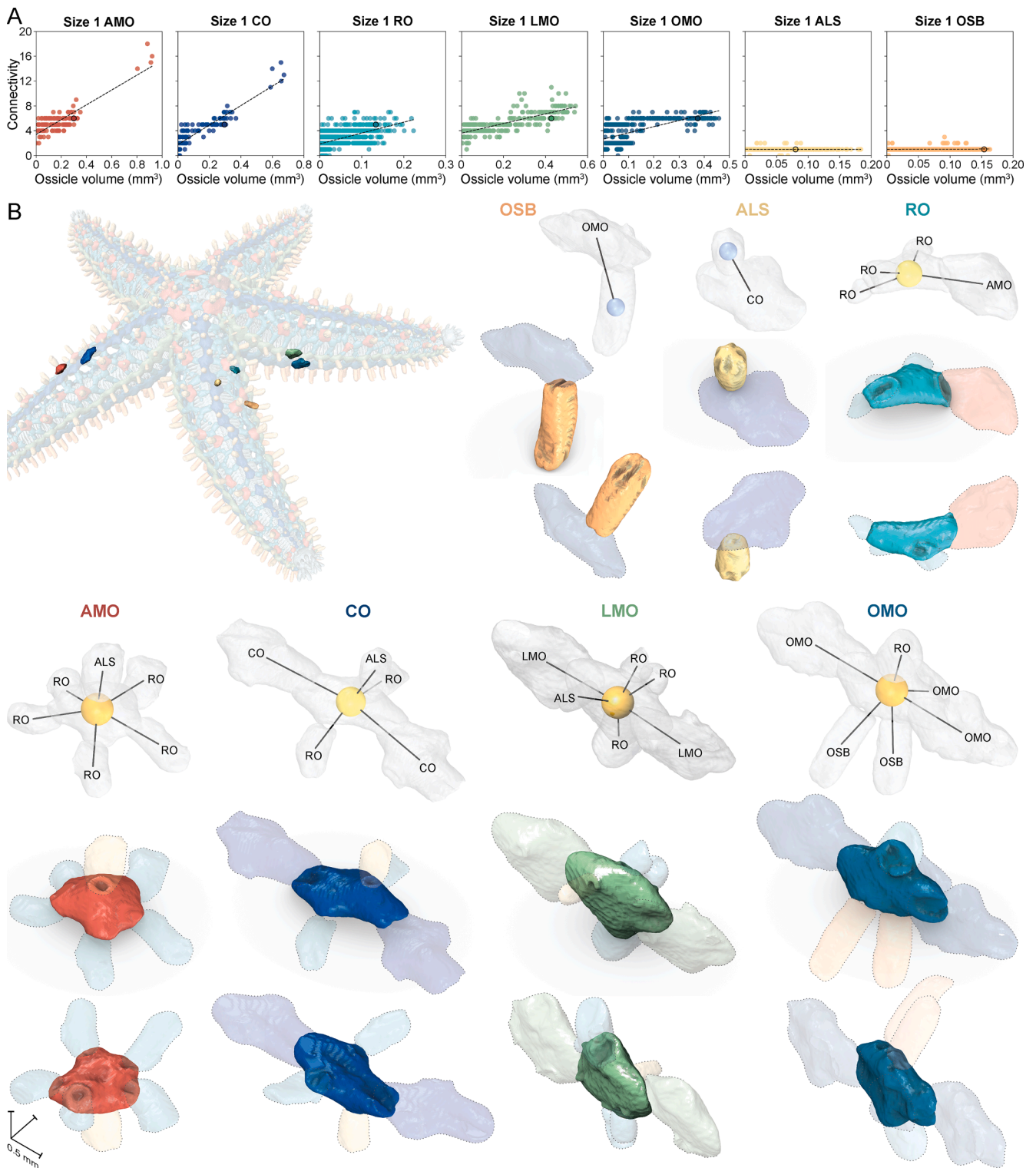
Fig. 11. Ossicle connectivity trends and connectivity-based sub-ossicle-scale morphological features. **A.** Scatter plots mapping individual ossicle volume against connectivity for each type of ossicle show clear trends (dotted line): an increase in ossicle volume is associated with an increase in connectivity (AMO, CO, RO, LMO, and OMO) or the connectivity remains constant (i.e., 1) regardless of ossicle volume (ALS and OSB). The data points for the ossicles shown in (B) are highlighted in the plots. **B.** Representative ossicles of each type, shown to scale in axonometric views, with their connectivity represented by color-coded spheres of weighted size (cf. Fig. 10A) (top row), their exterior faces (middle row) and interior faces (bottom row) exhibiting protrusions and depressions at the points of articulation with adjacent ossicles.

2019), and progressively decrease in size towards the tip of the arm (Eylers, 1976). They are connected together as to compose a series of structures not unlike the couples of a roof (Romanes, 1893), forming a

deep V-shaped groove on the oral surface of each arm (Eylers, 1976; Hyman, 1955; Nichols, 1966). The ossicles' thin, long, and ladle-like shape, and their arrangement in antimeric sets of ossicles form
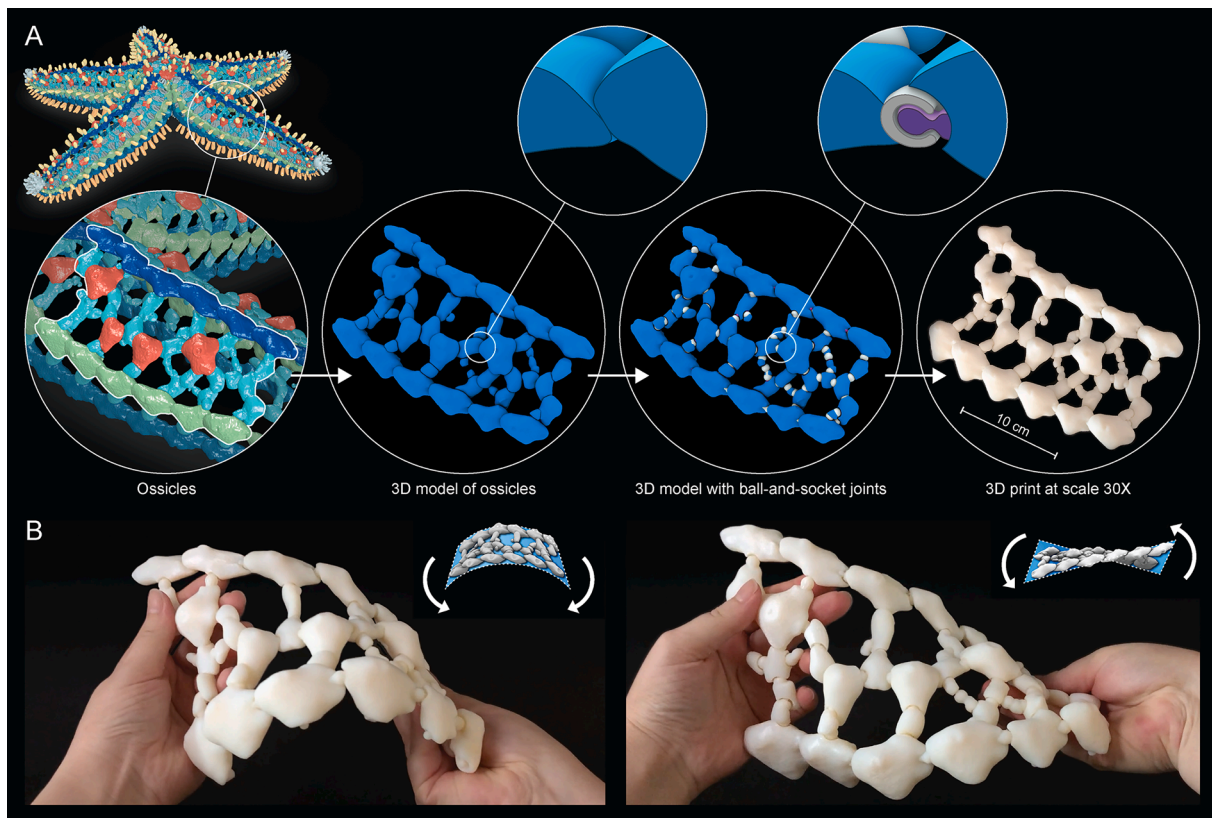
Fig. 12. 3D printed tangible models of interconnected ossicles from the smallest sea star in this study's growth series (Size 1). **A.** To generate the physical model, part of the skeletal system was first selected from the whole-animal data set. Our automated parametric modeling script then placed ball-and-socket joints at the locations where two ossicle geometries meet, and the resulting model was subsequently 3D printed at 30 times its original size. **B.** Photographs of the 3D-printed model held in two distinct positions, illustrating the considerable flexibility of the skeletal network during motions approximating lateral (in-plane) arm bending (left) and twisting (right).

alternating openings for the tube feet to pass through (Blowes et al., 2017; Eylers, 1976; Hyman, 1955; Lawrence, 1987; Meglitsch and Schram, 1991; Schwertmann et al., 2019). The ambulacral ossicles rest on the adambulacral ossicles (Eylers, 1976; Meglitsch and Schram, 1991), arranged in a single row on each side of the arm (Fig. 5A). These ossicles form a wall overhanging the ambulacral groove, increasing the depth of the groove and sheltering the tube feet (Lawrence, 1987), and each bear a small, slender oral spine that can be folded over the groove to provide additional protection (Hyman, 1955) (Fig. 5A). From our CT scans, we were also able to clearly distinguish the peristomal ring of fused ambulacral and adambulacral ossicles (Eylers, 1976; Hyman, 1955; Nichols, 1966) at the base of the arms (Fig. 2C). At the tips of the arms, we find the conspicuous terminal plates (Hyman, 1955), bearing spiny ornamentations (Fig. 2C and Fig. 3B). For the purpose of this study, which focused on the aboral skeletal ossicles and network, the ambulacral ossicles, adambulacral ossicles, small oral spines, the peristomal ring, and terminal plates were classified under the single label *Other*, unless otherwise specified.

The aboral portion of the skeleton forms an arch spanning between the two rows of adambulacral ossicles on either side of the arm (Eylers, 1976) (Fig. 5A). This aboral skeletal network consists of a lattice-like reticulum of more delicate ossicles (Eylers, 1976), which are very different in shape, size, and packing than seen in the oral skeleton, and can be most appreciated by looking at a virtual section of an arm (Fig. 5A). The bottom of the arch consists of chains of overlapping oral marginal ossicles (OMO), up to four chains wide, positioned adjacent to the adambulacral ossicles. The oral marginal ossicles each bear one to four big oral spines (OSB) (Fig. 5AB). These relatively long rod-like ossicles are movable and can either contact the substrate, or can close over the ambulacral groove to protect it when the animal is attacked (Barnes,

1987; Buchsbaum, 1947; Nichols, 1966). Above the oral marginal ossicles lays a single chain of overlapping lateral marginal ossicles (LMO) on each side of the arm (Fig. 5AB). These chains of oral marginal ossicles and lateral marginal ossicles slightly bend upward in the sea star's armpits before meeting with their respective chains in the adjacent arm. Collectively, these oral and lateral marginal ossicles have also been referred to as "marginal ossicles" (Blowes et al., 2017; Eylers, 1976; Schwertmann et al., 2019), or have been classified as "inferior marginals" (or "inframarginal ossicles") and "superior marginals" (or "supramarginal ossicles") (Hyman, 1955; Meglitsch and Schram, 1991; Nichols, 1966), respectively. The carinal ossicles (CO) run in a single ridge along the midline of the aboral skeleton (Eylers, 1976; Lawrence, 2013; Schwertmann et al., 2019), from the central disk to the tip of the arm, and are arranged like toppled dominoes (Blowes et al., 2017) (Fig. 3B and Fig. 5AB).

The highly repetitive chains of oral marginal ossicles, lateral marginal ossicles, and carinal ossicles, are connected to one another by a single or double-layer lattice-like structure of reticular ossicles (RO) (Fig. 3B and Fig. 5AB). The reticular ossicle organization rejects the bilateral skeletal symmetry followed by the other ossicle types, and is organized around circular voids in the body wall skeleton (Fig. 3B and Fig. 5AB). Within this irregular network of reticular ossicles, we also find scattered aboral marginal ossicles (AMO) (Fig. 3B and Fig. 5AB).

The network of reticular ossicles and aboral marginal ossicles continues over the aboral surface of the central disk, where we also find a few aboral marginal ossicles that are significantly larger and more distinctly shaped than those on the arms (Fig. 3B and Fig. 9B). Positioned slightly off-center and between two arms sits the largest and most lonesome ossicle of the sea star: the madreporite (Fig. 1E, Fig. 3B), or "madreporic tubercle" (Romanes, 1893), a button-shaped ossicle with

grooves and pores that draw in water and lead it into the sea star's water vascular system.

The lateral marginal ossicles, aboral marginal ossicles, carinal ossicles, and madreporite each support one or a few aboral lateral spines (ALS) (Fig. 3B), which are typically stubby and have a distinctive mushroom-like shape (see Fig. 5AB).

3.2. Ossicle quantity as a function of animal size

To better illustrate the abundance of ossicles in a single individual of *P. giganteus,* our high-throughput methodology includes the ability to arrange them in a two-dimensional matrix (Fig. 4). Even in the smallest sample of this study's growth series (Size 1), we identified an astounding 3,264 ossicles in the aboral skeleton. This visual representation also allows us to get a sense of the relative abundance of the different represented ossicle types, and provides a first impression of the diversity in ossicle shapes.

While unconfirmed, it has perhaps been generally accepted among echinoderm specialists that the number of ossicles increases as a sea star grows. Our high-throughput methodology allowed us to validate this theory for the first time. From the examination of virtual transverse arm sections, the continuous increase in ossicle number in the sea star skeletal system during growth first became apparent (Fig. 5AB), and was supported by analysis of the classified data sets: for the sea star specimens examined in this study, the total number of ossicles for each ossicle type was found to increase almost linearly with sea star diameter (Fig. 5C).

The most obvious increase is visible with the reticular ossicles (RO), growing from a single layer network in sea stars Size 1 through 3, to a double-layer network in Size 4 (Fig. 5A). As previously described by Fisher (1930) and depicted in Fig. 5A, as the animal grows, the skeleton is strengthened by the addition of elongate ossicles on the coelomic surface, especially in the form of buttresses on the sides of the ray. The result is a 13-fold increase in the number of reticular ossicles between Size 1 and Size 4 (Fig. 5C). In contrast, the ossicle types organized in single chains along the arm, i.e., the carinal ossicles (CO) and lateral marginal ossicles (LMO), naturally grow relatively little in number between Size 1 and Size 4, with roughly a mere 190% and 160% increase, respectively, as *P. giganteus* grows over seven times larger in diameter (Fig. 5C). In the transverse regions of interest that are positioned halfway along the arm, the number of chains of oral marginal ossicles (OMO) increases from two (Size 1 and 2), to three (Size 3), to four (Size 4) on each side of the arm (Fig. 5A). These observations corroborate the description by Hyman (1950), who remarked that towards the tips of the arms, the adambulacrals are in contact laterally with the inframarginals, while if the arms are broadly based, additional ossicles, two to five rows in *Pisaster* spp., are interposed between the adambulacrals and the inframarginals. The resulting increase in oral marginal ossicle numbers is 7.5-fold between Size 1 and Size 4 (Fig. 5C). Naturally, this increase is associated with roughly the same increase (6.5-fold) in the number of big oral spines (OSB) (Fig. 5C). The arm sections (Fig. 5AB) also show the abundance of both aboral marginal ossicles (AMO) and aboral lateral spines (ALS) in Size 4, compared to the smaller size sea stars. During sea star growth, the aboral marginal ossicles (AMO) appear to maintain a similar distance from one another on the reticulum (typically 3–6 mm) (Fig. 5AB), thus necessitating an increase in ossicle number as the arms grow in diameter. This observation was supported by the measured 12-fold increase in ossicle number between Size 1 and Size 4 (Fig. 5C). Since each aboral marginal ossicle bears one (or sometimes a few) aboral lateral spine(s) (ALS), the number of aboral lateral spines also increases appreciably (Fig. 5C).

When these numbers are expressed as a function of each sea star's surface area, we see a decrease in ossicle density as the sea star grows (Fig. 5D), thus demonstrating that the increase in individual ossicle volume (cf. Fig. 6) occurs at a proportionally faster rate than linear body growth.

3.3. Ossicle volumes: Arm position and changes during sea star growth

Individual ossicle volumes obtained from our workflow were used to both identify general trends in the sea star growth series and specific growth patterns for each ossicle type within a single sea star specimen.

Ossicle sizes in the aboral skeleton (excluding the madreporite) ranged from roughly $1.53 \bullet 10^{-4}$ mm^3 (a tiny reticular ossicle in Size 1, that had apparently formed only recently) to roughly 9.69 mm^3 (a large carinal ossicle in Size 4). On average, in a single sea star, the reticular ossicles (RO) are the smallest ossicles, and the aboral marginal ossicles (AMO), carinal ossicles (CO), and lateral marginal ossicles (LMO) are the largest ossicles in the aboral skeleton (excluding the madreporite) (Fig. 6). Furthermore, the average volume of each ossicle type was found to increase almost linearly with sea star diameter (Fig. 6A). These results suggest that, at least until a sea star reaches the dimensions of our Size 4 specimen, the ossicles of each type continue to increase in volume during sea star growth. To illustrate this point, representative ossicles of average volume were selected for each ossicle type from the Size 1, Size 3, and Size 4 sea stars, and are displayed in Fig. 6B.

As a sea star grows, new ossicles are generally added distally (Hyman, 1955), so in order to identify these or alternative ossicle growth patterns within a single sea star, ossicle volume and location data along the proximal–distal arm axis were obtained for each individual ossicle in a single arm, and plotted to identify potential trends.

As expected, based on general trends regarding skeletal anatomy in *P. giganteus* and other sea star species, our results demonstrate that ossicles of the same type are typically larger proximally, as indicated by the downward trend line toward the tip of the arm (e.g., ambulacral ossicles (AO)) or the downward trend in the upper boundary (e.g., reticular ossicles (RO)) formed by the scatter plots comparing distance from the sea star center point and ossicle volume (Fig. 7). A few ossicles positioned close to the base of the arms may also occasionally be smaller in size (e.g., Size 1 ALS, AMO, OSB), creating a slight upward curve before following the aforementioned downward trend (Fig. 7).

For some ossicle types, multiple trend lines can be identified. For example, the oral marginal ossicles (OMO) show two or more distinguishable size-location trends, corresponding with the number of adjacent chains of oral marginal ossicles on each side of the arm (Fig. 7). The plots also reveal that some of the chains, such as those positioned closer to the central arm axis, terminate well before reaching the arm tip (Fig. 7). In contrast to the oral marginal ossicles, the lateral marginal ossicles (LMO) are arranged in a single chain on each side of the arm, but also appear to show multiple trend lines (Fig. 7). Under closer examination, we were able to discern that the ossicles forming the upper trend line typically bear a spine and are (thus) generally larger, while the lower trend line is associated with the smaller ossicles that lack spines. In the more distal regions of the arms, these spine-bearing lateral marginal ossicles and those without are positioned alternately. The multiple trend lines that can be distinguished in the plots of some of the ossicle types hint at the presence of different ossicle subclasses, and were subsequently investigated in Section 3.5.

These plots also provide information on variation in ossicle size along the arm (Fig. 7). Low size variation, i.e., ossicle volumes following one or more relatively clear trend lines (e.g., LMO and AO), suggests that these ossicle types may only form at the arm tip, and continue to grow in place as the arm lengthens distally, while high size variation (e.g., ALS, AMO, and RO) suggests that these ossicle types may be formed at any point along the arm axis, between older ossicles, to accommodate the expanding diameter of the arms as the sea star grows.

3.4. Ossicle shape analyses as a function of ossicle volume and position

Upon an initial examination of the segmented and classified data sets, the distinct morphological characteristics of each ossicle type are already clearly visible. For example, the ambulacral ossicles (AO) are highly elongated and flattened, and the carinal ossicles (CO), lateral

marginal ossicles (LMO), and oral marginal ossicles (OMO) can be described as somewhat flattened and elongated ellipsoids, while the aboral marginal ossicles (AMO) can be compared to oblate spheroids. This variation in ossicle morphology between ossicle types is expected, and the observed geometric features are consistent with results reported from other asteroids (Blowes et al., 2017; Eylers, 1976; O'Neill, 1989; Turner and Dearborn, 1972; Schwertmann et al., 2019).

However, as has been described in other species (Blowes et al., 2017; Turner and Dearborn, 1972; Schwertmann et al., 2019), we observed that ossicle shape can also often vary within a specific ossicle type. The most striking example is for the reticular ossicles, which consist of a wide range of morphologically distinct ossicle types (Fig. 4) that have been grouped based on their function as bridging ossicles within the skeletal matrix (Fig. 5AB). While the reticular ossicles represent extreme morphological variation, other ossicle types clearly exhibit location-specific morphological and size trends. For example, the shape of an oral marginal ossicle (OMO) is more elongated on the chains positioned on the outer surface, whereas ossicles on the inner chains were comparatively shorter. We also discovered that the more distal ossicles of most types, which are inherently smaller in size, are relatively thicker and more square-shaped in plan view. This trend was particularly evident for the aboral marginal ossicles (AMO), lateral marginal ossicles (LMO), oral marginal ossicles (OMO), and carinal ossicles (CO).

These observations raised intriguing questions as to the relationship between ossicle shape, volume, and their relative arm positions. Since our high-throughput workflow allowed us to obtain shape data on all the ossicles present in a whole sea star, we were able to perform these analyses on a large data set of ossicles, and identify potential trends. In terms of ossicle elongation and flatness, the results of our analysis of the reticular ossicles (RO), lateral marginal ossicles (LMO), and ambulacral ossicles (AO) in a single arm of the smallest sea star (Size 1), which reveal no, some, and high correlation, respectively, are shown in Fig. 8. Due to the extraordinary diversity in reticular ossicle shape, as illustrated in a few samples viewed in axonometric perspective (Fig. 8A, top), with elongations ranging from 0.12 to 0.94, and flatnesses ranging from 0.22 to 0.96, there is a complete absence of any correlation between ossicle shape and ossicle volume, or ossicle shape and distance from the sea star center point (Fig. 8A). The lateral marginal ossicles, an example of a type of ossicles arranged in a single chain along the arm, show some trends regarding ossicle flatness and ossicle volume or location, although the ossicles still exhibit noticeable diversity in shape (Fig. 8B). The ambulacral ossicles, in contrast, show exceptionally high correlation between ossicle shape and ossicle volume or location (Fig. 8C), reflected in a gradual decline in volume towards the arm tip and their relatively constant shape, with an elongation and flatness ranging between roughly 0.05 and 0.10, and 0.17 and 0.52, respectively (Fig. 8C).

3.5. Ossicle subclassification based on size, shape, and location

As shown in Fig. 7, some ossicle types exhibit significant variation in size, and from examination of these data, the different ossicle types can be divided into one of three distinct categories: either those whose variability exhibits no predictable correlation as a function of arm location, those that exhibit a single growth trend, or those that exhibit multiple distinguishable growth trends. These observations were further supported by the non-normal distribution of ossicle volumes, revealed in violin plots for each ossicle type (Fig. 9A). Along with the significant differences in shape (Section 3.4, Fig. 8), for some ossicle types these observations led us to consider the existence of distinct subclasses within the eight main aboral ossicle groupings we identified during our initial ossicle classification (i.e., ALS, AMO, CO, LMO, OMO, OSB, RO, and the madreporite).

To explore this possibility, we applied classification algorithms to our ossicle volume and ossicle location data sets, including those of the oral marginal ossicles (OMO), and aboral marginal ossicles (AMO) of the

Size 3 sea star. The support vector clustering algorithm (Pedregosa et al., 2011) was able to distinguish oral marginal ossicles belonging to the three different chains (Fig. 9B), and violin plots for each of the three subclasses revealed that the uppermost peak in the original violin plot was formed by the ossicles in the outer chains, and the middle and lower peaks primarily by the ossicles in the middle and inner chains. In the aboral marginal ossicles, an agglomerative clustering algorithm (Pedregosa et al., 2011) identified three subclasses (Fig. 9B), the most conspicuous of which consisted of the four significantly larger aboral marginal ossicles positioned on the central disk. The two other subclasses are less conspicuous, the first one consisting of larger ossicles on the central disk and the proximal region of the arms, and the second of smaller ossicles positioned on the arm tips.

In addition to ossicle volume and location, ossicle shape (i.e., elongation and flatness) was also used as a criteria to investigate the potential existence of morphologically distinct ossicle subclasses. In the case of the lateral marginal ossicles (LMO), for example, the support vector clustering algorithm identified two subclasses, the first consisting of the ossicles positioned in each armpit, and the second of the remaining ossicles in the chains along each side of the arm (Fig. 9C).

3.6. Modeling skeletal network connectivity to understand sub-ossicle-scale morphological features

To better understand large-scale ossicle organizational patterns and their relationship with individual ossicle morphologies, we developed methods for the creation of whole sea star-level ossicle connectivity network diagrams. This approach allowed us to visualize the number of connections each ossicle makes with its adjacent ossicles (Fig. 10A), and from these measurements, we found that aboral ossicles with the highest number of connections are typically positioned in the armpits or on the central disc.

These data also allowed us to calculate nearest neighbor connectivity frequencies, and revealed that the majority of ossicle connections present in the sea star (roughly 28%) are between reticular ossicles (RO-RO), followed by connections between reticular ossicles and lateral marginal ossicles (RO-LMO), reticular ossicles and aboral marginal ossicles (RO-AMO), and oral marginal ossicles and big oral spines (OMO-OSB), with roughly 13%, 12%, and 12%, respectively (Fig. 10B). It should be noted that the connections tallied between spines (aboral lateral spines (ALS) and big oral spines (OSB)) and spines of the same group (ALS-ALS or OSB-OSB) or other ossicles (ALS-RO, ALS-OMO) can potentially be misleading, given that spines are movable and/or may be oriented towards a nearby ossicle, and may thus be in close proximity to an ossicle to which it is not physically connected.

The information on ossicle connectivity also provides clues as to the function of specific sub-ossicle-scale morphological features. For example, the data set acquired from the smallest sea star (Size 1) was of a sufficiently high resolution to clearly identify smaller-scale ossicle morphological features at the points of connections with adjacent ossicles. Our first study, using a series of aboral marginal ossicles of different connectivities (4, 5, 6, and 9) shows how each ossicle sits atop adjacent reticular ossicles (RO) and provides one connection to an aboral lateral spine (ALS) on the opposite side. The ossicles exhibit protrusions in the regions at which they connect to the reticular ossicles, the number of which is closely correlated with the overall ossicle polygonal form, as previously observed by Schwertmann et al. (2019). This pattern leads, for example, to an approximately triangular base if the ossicle connects to three reticular ossicles, and an approximately pentagonal base if the ossicle connects to five reticular ossicles, the results of which were used to validate our global connectivity predictions. Upon closer examination, we could also identify joint-like features, consisting of roughly circular depressions (or "grooves" (Schwertmann et al., 2019)), or "alveoli" surrounded by "articulation ridges" (Turner and Dearborn, 1972)) in the regions where an aboral marginal ossicle connects to its aboral lateral spine (ALS), or overlaps with adjacent reticular ossicles

(RO) (Fig. 10B). Based on descriptions of interossicular attachment (Blowes et al., 2017; Eylers, 1976; Motokawa, 1985, 1986; O'Neill, 1989; Turner and Dearborn, 1972), and as suggested by Schwertmann et al. (2019), these joint-like depressions likely provide a large surface area for the attachment of interossicular musculature and collagen fibers, and might further allow for a closer positioning of adjoining ossicles during the formation of rigid jamming postures.

The aboral marginal ossicle data depicted in Fig. 10B also suggest that ossicle volume increases as a function of the number of adjacent ossicles to which it is connected. Hence, we subsequently set out to investigate this potential relationship in the aboral ossicle types. The positive correlation can easily be recognized in the aboral marginal ossicles (AMO), and the single-chained carinal ossicles (CO) and lateral marginal ossicles (LMO) (Fig. 11A). The relationship is less conspicuous, and is perhaps even non-existent, in the reticular ossicles (RO) and oral marginal ossicles (OMO) (Fig. 11A). The latter is likely the result of their arrangement in multiple adjacent chains, and more apparent correlations between volume and connectivity could be expected if each identified subclass of the oral marginal ossicles (Fig. 9B) were analyzed individually. Lastly, regardless of ossicle volume, only one connection is formed between a spine (ALS or OSB) and another ossicle (Fig. 11A) (although the data includes a few ossicles with zero connections, likely a result of thicker soft tissue separating the spine and its adjacent ossicle, thus preventing the software from detecting a connection, and two connections, resulting from the aforementioned inaccuracy in the automated computing of spine connections).

In addition, our aforementioned analysis of the aboral marginal ossicles suggest a strong correlation between ossicle shape, sub-ossicle-scale morphological features, and the number of connections with adjacent ossicles (Fig. 10B), which can potentially be extrapolated to infer similar relationships for other ossicle types. For example, if we compare the two spine types from *P. giganteus*, we observe similar articulation point geometries for adjacent ossicles. The big oral spines (OSB) exhibit a long linear groove at the point of attachment to an oral marginal ossicle (OMO), which, in turn, feature a similar linear groove. In contrast, the aboral lateral spines (ALS), similar to the non-spine ossicles, feature a circular depression in the zone of contact with an adjacent ossicle (Fig. 11B).

As mentioned previously, while the reticular ossicle (RO) morphologies are as diverse as the number and orientation of their connections (Fig. 4 and Fig. 11A), like the aboral marginal ossicles, they also exhibit small depressions at the points of contact with their neighbors (Fig. 11B).

Ossicles that are organized into chains, i.e., the carinal ossicles (CO), lateral marginal ossicles (LMO), and oral marginal ossicles (OMO), overlap one another on their proximal and distal ends, and the more elongated shape in the direction of the arm axis establishes a greater contact surface between these ossicles (Fig. 11B). In the areas where the ossicles overlap, the ossicles become significantly flatter and feature the typical depressions for ossicle-ossicle connections (Fig. 11B). In contrast to the depressions found in the aboral marginal ossicles, those in the chain-forming ossicles (CO, LMO, OMO), which provide a connection to ossicles of the same type, are relatively large and sometimes more elongated. Yet, similar to the aboral marginal ossicles, these ossicles exhibit protrusions in the areas where they connect to adjacent ossicles, giving the ossicles their distinctive geometries. For example, the carinal ossicles (CO) connect to adjacent carinal ossicles longitudinally, while connecting to other ossicles (often reticular ossicles) laterally, and an aboral lateral spine (ALS) in the aboral direction, leaving them with a cross-like geometry, and a slight thickening at the position of the spine (Fig. 6B and 11B). The lateral marginal ossicles (LMO) also connect with adjacent ossicles of the same type in the proximal–distal direction, while connecting in the oral-aboral direction with other ossicles, and, in some cases, in the lateral direction with aboral lateral spines (Fig. 11B).

3.7. Skeletal network: Flexibility

As shown in this study, while micro-CT-derived data sets can be extremely useful for the identification and analysis of different ossicle types and their distinctive geometric features, they provide limited information regarding the role of the dermal skeletal system in global arm kinematics, leading to mostly qualitative descriptions of skeletal mechanics, similar to those provided in previous studies (Blowes et al., 2017; O'Neill, 1989, 1990; Schwertmann et al., 2019).

Leveraging the data on ossicle geometry, organization, and connectivity obtained through our Amira-based workflow, we developed an automated parametric modeling script that allows us to generate fully articulated 3D-printable models of the skeletal system (Fig. 12A). The incorporation of ball-and-socket joints between adjacent ossicles, which were used to approximate local ossicle-ossicle interactions, can thus be used to explore complex skeletal deformations in 3D space (Video 1) and provide valuable insights into the relative motions of the ossicles that enable arm bending and twisting (Fig. 12B).

4. Discussion

As described in the present study, we have developed a new segmentation and data processing workflow that allows for the high-throughput multi-scale analysis of complex multi-component skeletal systems. By employing a combination of micro-CT imaging, automated segmentation and classification, data visualization, and additive manufacturing, we have demonstrated the value of this approach for investigating the complex dermal endoskeletal network from the giant knobby star, *P. giganteus*, and its changes as a function of animal growth, at both whole-animal and single-ossicle length scales.

In contrast to more traditional manual segmentation-based approaches, this automated alternative removes experimenter bias (Schwertmann et al., 2019) and allows for whole-animal-level analyses, which have previously been incredibly labor-intensive, and thus for all practical purposes, unachievable. While the current study was performed on only four different individuals as a proof of concept, the automated nature of this workflow could be applied to examine a much larger number of specimens. Including additional individuals could help reduce potential sampling errors and allow for a much more detailed growth series to be explored, from mapping the complete ontogenetic development of a sea star skeleton during larvae metamorphosis when the skeletal system appears (Barnes, 1987; Nichols, 1966), to sea star "giants" measuring over 60 cm in diameter. The results from these studies could thus provide critical insights into skeletal network scaling laws and could subsequently be used to directly infer relative ranges of body/arm motion during different stages of growth.

From a biodiversity and evolutionary perspective, since ossicle architecture plays a critical role in the identification of species and for inferring evolutionary relationships between echinoderms (Pisera and Dzik, 1979; Feder, 1980), this high-throughput methodology could also be employed for phylogenetic analyses and for the identification of potential subspecies (Jangoux, 2022). While many conventional classification schemes are based on the characteristics of individual ossicles (Feder, 1980; Sladen, 1886; Mah and Blake, 2012), there's a call for caution in the interpretation of isolated ossicles for inferring evolutionary relationships (Blake and Portell, 2009), especially for taxa where the whole-animal skeletal architecture is poorly understood. Thus, the ability to reliably depict the spatial relationships of the constituent skeletal elements in the mature skeletal systems is critical. As such, its ability to efficiently clarify network connectivity in complex skeletal systems and obtain data on morphological features of the entire repertoire of skeletal elements in a given individual makes our methodology ideally suited for comparing closely or distantly related species.

At the ecological level, the extent of asteroid skeletal development has been linked to arm robustness and flexibility (Blake, 1989), and consequently, species-specific feeding modes (Feder, 1980). The

capability of the presented methodology to rapidly segment entire skeletal systems provides an important stepping stone toward understanding correlations between skeletal architecture and, for example, strength, speed, and agility, and evolutionary kinematic trade-offs between them. Moreover, while mechanical stresses in the asteroid skeletal system have previously been examined analytically and experimentally (Eylers, 1976; O'Neill, 1990), our methodology can be expanded to allow for future biomechanical studies to investigate mechanical stress distribution within the whole skeletal structure in detail, possible correlations between ossicle shape and biomechanical stresses, and the mechanical consequences of large-scale ossicle jamming, a principle that has recently gained considerable interest in the biologically inspired grasping community (Brown et al., 2010; Jeong et al., 2019). Furthermore, the ability to generate fully interactive 3D-printable articulated skeletal systems using our ball-and-socket joint algorithms, can further complement these investigations, by providing tangible interfaces for hypothesis testing. These 3D-printed models also provide a valuable resource for investigating structure–function relations in sea star skeletal systems in an educational context.

Future efforts will largely focus on the development and optimization of automated ossicle classification workflows that were explored during the early stages of this study. By employing machine learning algorithms and targeting location-specific, and morphologically-specific ossicle features such as volume and shape, as well as the number of connections with adjacent ossicles, the methodologies described in the present study could be significantly streamlined, further decreasing the time frames required to complete the ossicle classification process. Furthermore, it should be noted that while the methodologies presented herein were coded and executed using Amira and Rhinoceros/Grasshopper, the recent development of custom workflows for performing biological shape analysis of juxtaposed and/or serially repeating skeletal elements within open source programming environments such as 3D Slicer (Diaz-Pinto et al., 2022; Fedorov et al., 2012; Rolfe et al., 2021; Wasserthal et al., 2022) could potentially be adapted to perform automated segmentation functions similar to the methodology presented here.

Since the workflows presented here were organized around investigating the dermal endoskeletons of sea stars, which rank among the most morphologically diverse and structurally complex skeletal systems in the animal kingdom, these approaches should likely find great utility in the investigation of other tessellated or dispersed-element-based skeletal systems, with examples such as crinoid and holothuroid endoskeletons, gorgonian sclerites, sponge spicules, larval caddisfly tubes, chiton girdle scales, mollusk radulae, fish scales, elasmobranch cartilage, and reptile osteoderms. As such, these high-throughput methodologies that utilize an information-rich programming environment thus have the potential to revolutionize the fields of comparative skeletal anatomy and mechanics in these notoriously challenging and problematic multi-component skeletal architectures.

CRediT authorship contribution statement

Lara Tomholt: Methodology, Investigation, Data curation, Visualization, Writing – original draft, Writing – review & editing. **Daniel Baum:** Methodology, Investigation, Data curation, Visualization, Writing – original draft, Writing – review & editing. **Robert J. Wood:** Funding acquisition, Writing – review & editing. **James C. Weaver:** Funding acquisition, Conceptualization, Supervision, Methodology, Investigation, Data curation, Visualization, Writing – original draft, Writing – review & editing.

Declaration of Competing Interest

The authors declare that they have no known competing financial interests or personal relationships that could have appeared to influence the work reported in this paper.

Data availability

Data will be made available on request.

Appendix A. Supplementary data

Supplementary data to this article can be found online at https://doi.org/10.1016/j.jsb.2023.107955.

References

Barnes, R.D., 1987. Invertebrate zoology. Saunders College Publishing, Philadelphia.

Baum, D., Weaver, J.C., Zlotnikov, I., Knötel, D., Tomholt, L., Dean, M.N., 2019. High-throughput segmentation of tiled biological structures using random-walk distance transforms. Integrative and Comparative Biology 59 (6), 1700–1712. https://doi.org/10.1093/icb/icz117.

Blake, D.B., 1989. Asteroidea: functional morphology, classification and phylogeny. In: Jangoux, M., Lawrence, J.M. (Eds.), Echinoderm studies, 3. A.A. Balkema, Rotterdam, pp. 179–223.

Birenheide, R., Yokoyama, K., Motokawa, T., 2000. Cirri of the stalked crinoid Metacrinus rotundus: neural elements and the effect of cholinergic agonists on mechanical properties. Proceedings of the Royal Society B 267, 7–16. https://doi.org/10.1098/rspb.2000.0959.

Blake, D.B., Portell, R.W., 2009. Implications for the study of fossil Asteroidea (Echinodermata) of new genera and species from the eocene of Florida. Journal of Paleontology 83 (4), 562–574. https://doi.org/10.1666/08-097R.1.

Blowes, L.M., Egertová, M., Liu, Y., Davis, G.R., Terril, N.J., Gupta, H.S., Elphick, M.R., 2017. Body wall structure in the starfish Asterias rubens. Journal of Anatomy 231, 325–341. https://doi.org/10.1111/joa.12646.

Breiman, L., 2001. Random Forests. Machine Learning 45, 5–32.

Brown, E., Rodenberg, N., Amend, J., Mozeika, A., Steltz, E., Zakin, M.R., Lipson, H., Jaeger, H.M., 2010. Universal robotic gripper based on the jamming of granular material. PNAS 107 (44), 18809–18814. https://doi.org/10.1073/pnas.1003250107.

Buchsbaum, R.M., 1947. Animals without backbones; and introduction to the invertebrates. University of Chicago Press, Chicago.

Diaz-Pinto, A., Alle, S., Ihsani, A., Asad, M., Nath, V., Pérez-García, F., Mehta, P., Li, W., Roth, H.R., Vercauteren, T., Xu, D., Dogra, P., Ourselin, S., Feng, A., Cardoso, M.J., 2022. MONAI Label: a framework for AI-assisted interactive labeling of 3D medical images. *arXiv.* https://doi.org/10.48550/arXiv.2203.12362.

Dubois, P., Jangoux, M., 1985. The microstructure of the asteroid skeleton (*Asterias rubens*). *Proceedings of the Fifth International Echinoderm Conference, Galway, 24-29 September 1984.* pp.507-512. https://doi.org/10.1201/9781003079224-105.

Emson, R.H., 1985. Bone idle - a recipe for success? *Proceedings of the Fifth International Echinoderm Conference, Galway, 24-29 September 1984.* pp.25-30. https://doi.org/10.1201/9781003079224-5.

Eylers, J.P., 1976. Aspects of skeletal mechanics of the starfish *Asterias forbesii*. Journal of Morphology 149 (3), 353–368. https://doi.org/10.1002/jmor.1051490305.

Feder, H.M., 1980. Asteroidea: the sea stars. In: Morris, R.H., Abbott, D.P., Haderlie, E.C. (Eds.), Intertidal Invertebrates of California. Stanford University Press, Stanford, California, pp. 117–135.

Fedorov, A., Beichel, R., Kalpathy-Cramer, J., Finet, J., Fillion-Robin, J.-C., Pujol, S., Bauer, C., Jennings, D., Fennessy, F.M., Sonka, M., Buatti, J., Aylward, S.R., Miller, J. V., Pieper, S., Kikinis, R., 2012. 3D Slicer as an image computing platform for the quantitative imaging network. Magnetic Resonance Imaging 30 (9), 1323–1341. https://doi.org/10.1016/j.mri.2012.05.001.

Fisher, W.K. (1930). Asteroidea of the North Pacific and Adjacent Waters, Pt. 3: Forcipulata (Concluded). *Bulletin of the United States National Museum 76.* 1-356. Pls. 1-93.

Frølich, S., Weaver, J.C., Dean, M.N., Birkedal, H., 2017. Uncovering nature's design strategies through parametric modeling, multi-material 3D printing, and mechanical testing. Advanced Engineering Materials 19 (6), 1600848. https://doi.org/10.1002/adem.201600848.

Gayathri, S., Lakshminarayanan, R., Weaver, J.C., Morse, D.E., Kini, R.M., Valiyaveettil, S., 2007. In vitro study of magnesium-calcite biomineralization in the skeletal materials of the seastar *Pisaster giganteus. Chemistry. A European Journal*, 13, pp.32-62-3268. https://doi.org/10.1002/chem.200600825.

Hayne, K.J.R., Palmer, A.R., 2013. Intertidal sea stars (*Pisaster ochraceus*) alter body shape in response to wave action. The Journal of Experimental Biology 216, 1717–1725. https://doi.org/10.1242/jeb.078964.

Hyman, L.H., 1955. The invertebrates: Echinodermata (Vol. McGraw-Hill Book Company, New York, IV).

Jangoux, M., 2022. The type specimens of extant asteroids (Echinodermata) in the Muséum national d'Histoire naturelle of Paris. Zoosystema 44 (11), 259–334.

Jeong, H.,Kim, J. 2019. Echinoderm inspired variable stiffness soft actuator with connected ossicle structure. *2019 International Conference on Robotics and Automation (ICRA), Palais des congres de Montreal, Montreal, Canada, May 20-24.* pp. 7389-7394. https://doi.org/10.1109/ICRA.2019.8793545.

Jones, A., 1935. 2019. Analysis of aboral spine variation in the forcipulate sea star, Pisaster ochraceus (Brandt.

Lawrence, J., 1987. A functional biology of echinoderms. The John Hopkins University Press, Baltimore.

Lawrence, J.M., 2013. The asteroid arm. In: Lawrence, J.M. (Ed.), Starfish. The Johns Hopkins University Press, Baltimore, Biology and ecology of the asteroidea, pp. 15–23.

LeClair, E.E., LaBarbara, M.C., 1997. An in vivo comparative study of intersegmental flexibility in the ophiuroid arm. Biological Bulletin 193, 77–89. https://doi.org/10.2307/1542737.

Mah, C.L., Blake, D.B., 2012. Global diversity and phylogeny of the Asteroidea (Echinodermata). PLoS ONE 7 (4), e35644.

Meglitsch, P.A., Schram, F.R., 1991. Invertebrate Zoology. Oxford University Press, Oxford.

Motokawa, T., 1984. Connective tissue catch in echinoderms. Biological Reviews 59, 255–270. https://doi.org/10.1111/j.1469-185X.1984.tb00409.x.

Motokawa, T., 1986. Morphology of spines and spine joint in the crown-of-thorns starfish *Acanthaster planci* (Echinodermata, Asteroida). Zoomorphology 106, 247–253. https://doi-org.ezp-prod1.hul.harvard.edu/10.1007/BF00312046.

Motokawa, T., 2011. Mechanical mutability in connective tissue of starfish body wall. Biological Bulletin 221, 280–289. https://doi.org/10.1086/BBLv221n3p280.

Motokawa, T., Wainwright, S.A., 1991. Stiffness of starfish arm and involvement of catch connective tissue in the stiffness change. Comparative biochemistry and physiology. A, Comparative physiology 100 (2), 393–397. https://doi.org/10.1016/0300-9629(91)90489-Y.

Motokawa, T., 1985. Catch connective tissue: the connective tissue with adjustable mechanical properties. In: Keegan, B.F., O'Connor, B.D.S. (Eds.) *Echinodermata: proceedings of the fifth International Echinoderm Conference, Galway, 24-29 September 1984*, pp.69-74. https://doi.org/10.1201/9781003079224-9.

Motokawa, T., 1988. Catch connective tissue: a key character for echinoderms' success. In: Burke, R.D., Mladenov, P.V., Lambert, P., Parsley, R.L. (Eds.) *Echinoderm biology: proceedings of the sixth International Echinoderm Conference, Victoria, 23-28 August 1987*, pp.39-54. Balkema, Rotterdam.

Nichols, D., 1966. Echinoderms. Hutchinson & Co Ltd, London.

O'Neill, P., 1989. Structure and mechanics of starfish body wall. Journal of experimental biology 147, 53–89. https://doi.org/10.1242/jeb.147.1.53.

O'Neill, P., 1990. Torsion in the Asteroid Ray. Journal of Morphology 203, 141–149. https://doi.org/10.1002/jmor.1052030203.

Pedregosa, F., Varoquaux, G., Gramfort, A., Michel, V., Thirion, B., Grisel, O., Blondel, M., Prettenhofer, P., Weiss, R., Dubourg, V., Vanderplas, J., Passos, A., Cournapeau, D., Perrot, M., Duchesnay, É., 2011. Scikit-learn: machine learning in Python. Journal of Machine Learning Research 12, 2825–2830.

Pisera, A., Dzik, J., 1979. Tithonian crinoids from Rogźnik (Pieniny Klippen Belt, Poland) and their evolutionary relationships. Eclogae Geologicae Helvetiae 72, 805–849.

Robles, C., 2013. Pisaster ochraceus. In: Lawrence, J.M. (Ed.), Starfish. The Johns Hopkins University Press, Baltimore, Biology and ecology of the asteroidea, pp. 161–173.

Roediger, L.M., Bolton, T.F., 2008. Abundance and distribution of South Australia's endemic sea star, Parvulastra parvivipara (Asteroidea: Asterinidae). Marine and Freshwater Research. 59 (3), 205–213. https://doi.org/10.1071/MF07084.

Rolfe, S., Pieper, S., Porto, A., Diamond, K., Winchester, J., Shan, S., Kirveslahti, H., Boyer, D., Summers, A., Maga, A.M., 2021. SlicerMorph: An open and extensible platform to retrieve, visualize and analyse 3D morphology. Methods in Ecology and Evolution 12 (10), 1816–1825. https://doi.org/10.1111/2041-210X.13669.

Romanes, G.J., 1893. Jelly-fish, star-fish, and sea-urchins. Being a research on primitive nervous systems, International scientific series, New York, NY.

Sanford, E., 2002. The feeding, growth, and energetics of two rocky intertidal predators (*Pisaster ochraceus* and *Nucella canaliculata*) under water temperatures simulating episodic upwelling. Journal of Experimental Marine Biology and Ecology 273 (2), 199–218. https://doi.org/10.1016/S0022-0981(02)00164-8.

Sladen, P. 1886. *Report on the asteroidea (starfish) collected by H.M.S. Challenger during the years 1873-1876.* (Report on the scientific results of the voyage of H.M.S. Challenger during the years 1873-76. Zoology Vol. 30, Part 51) HMSO, London.

Schwertmann, L., Focke, O., Dirks, J.-H., 2019. Morphology, shape variation and movement of skeletal elements in starfish (*Asterias rubens*). Journal of Anatomy 234, 656–667. https://doi.org/10.1111/joa.12964.

Smith, A.B., 1990. Biomineralization in Echinoderms. In: Carter, J.G. (Ed.), Skeletal biomineralization: patterns, processes and evolutionary trends, Volume 1. Van Nostrand Reinhold, New York, pp. 413–443.

Tomholt, L., Friesen, L.J., Berdichevsky, D., Fernandes, M.C., Pierre, C., Wood, R.J., Weaver, J.C., 2020. The structural origins of brittle star arm kinematics: An integrated tomographic, additive manufacturing, and parametric modeling-based approach. Journal of Structural Biology 211 (1), 107481. https://doi.org/10.1016/j.jsb.2020.107481.

Turner, R.L., Dearborn, J.H., 1972. Skeletal morphology of the mud star, Ctenodiscus crispatus (Echinodermata: Asteroidea). Journal of Morphology 138, 239–262. https://doi.org/10.1002/jmor.1051380207.

Wasserthal, J., Meyer, M., Breit, H.-C., Cyriac, J., Yang, S., Segeroth, M., 2022. TotalSegmentator: robust segmentation of 104 anatomical structures in CT images. *arXiv*. https://doi.org/10.48550/arXiv.2208.05868.

Wilkie, I.C., 2005. Mutable collagenous tissue: overview and biotechnological perspective. In: Matranga, V. (Ed.), *Echinodermata. Progress in Molecular and Subcellular Biology (Marine Molecular Biotechnology)*, vol 39. Springer, Berlin, pp. 221–250. https://doi.org/10.1007/3-540-27683-1_10.

Wood, J.G., 1898. Animate Creation. Selmar Hess, New York.

Yang, T., Chen, H., Jia, Z., Deng, Z., Chen, L., Peterman, E.M., Weaver, J.C., Li, L., 2022. A damage-tolerant, dual-scale, single-crystalline microlattice in the knobby starfish. Protoreaster nodosus. *Science* 375 (6581), 647–652. https://doi.org/10.1126/science.abj9472.